Measurement of J/ψ at forward and backward rapidity in p + p, p + Al, p + Au, and 3 He +Au collisions at √sNN = 200 GeV

(PHENIX Collaboration) Acharya, U.; ...; Makek, M.; ...; Vukman, N.; ...; Zou, L.

Measurement of J/ψ at forward and backward rapidity in $p+p$, $p+$Al, $p+$Au, and ^{3}He$+$Au collisions at $\sqrt{s_{NN}} = 200$ GeV

U. Acharya,[21] A. Adare,[12] C. Aidala,[42] N. N. Ajitanand,[60,*] Y. Akiba,[55,56,†] M. Alfred,[23] V. Andrieux,[42] N. Apadula,[28,61] H. Asano,[35,55] B. Azmoun,[7] V. Babintsev,[24] M. Bai,[6] N. S. Bandara,[41] B. Bannier,[61] K. N. Barish,[8] S. Bathe,[5,56] A. Bazilevsky,[7] M. Beaumier,[8] S. Beckman,[12] R. Belmont,[12,42,48] A. Berdnikov,[58] Y. Berdnikov,[58] D. S. Blau,[34,45] M. Boer,[37] J. S. Bok,[47] K. Boyle,[56] M. L. Brooks,[37] J. Bryslawskyj,[5,8] V. Bumazhnov,[24] S. Campbell,[13,28] V. Canoa Roman,[61] R. Cervantes,[61] C.-H. Chen,[56] C. Y. Chi,[13] M. Chiu,[7] I. J. Choi,[25] J. B. Choi,[30,*] T. Chujo,[64] Z. Citron,[66] M. Connors,[21,56] N. Cronin,[43,61] M. Csanád,[16] T. Csörgő,[17,67] T. W. Danley,[49] A. Datta,[46] M. S. Daugherity,[1] G. David,[7,15,61] K. DeBlasio,[46] K. Dehmelt,[61] A. Denisov,[24] A. Deshpande,[7,56,61] E. J. Desmond,[7] A. Dion,[61] P. B. Diss,[40] D. Dixit,[61] J. H. Do,[68] A. Drees,[61] K. A. Drees,[6] J. M. Durham,[37] A. Durum,[24] A. Enokizono,[55,57] H. En'yo,[55] R. Esha,[61] S. Esumi,[64] B. Fadem,[43] W. Fan,[61] N. Feege,[61] D. E. Fields,[46] M. Finger,[9] M. Finger, Jr.,[9] D. Fitzgerald,[42] S. L. Fokin,[34] J. E. Frantz,[49] A. Franz,[7] A. D. Frawley,[20] Y. Fukuda,[64] C. Gal,[61] P. Gallus,[14] E. A. Gamez,[42] P. Garg,[3,61] H. Ge,[61] F. Giordano,[25] A. Glenn,[36] Y. Goto,[55,56] N. Grau,[2] S. V. Greene,[65] M. Grosse Perdekamp,[25] T. Gunji,[11] H. Guragain,[21] T. Hachiya,[44,55,56] J. S. Haggerty,[7] K. I. Hahn,[18] H. Hamagaki,[11] H. F. Hamilton,[1] S. Y. Han,[18,33,55] J. Hanks,[61] S. Hasegawa,[29] T. O. S. Haseler,[21] K. Hashimoto,[55,57] X. He,[21] T. K. Hemmick,[61] J. C. Hill,[28] K. Hill,[12] A. Hodges,[21] R. S. Hollis,[8] K. Homma,[22] B. Hong,[33] T. Hoshino,[22] N. Hotvedt,[28] J. Huang,[7] S. Huang,[65] K. Imai,[29] M. Inaba,[64] A. Iordanova,[8] D. Isenhower,[1] S. Ishimaru,[44] D. Ivanishchev,[53] B. V. Jacak,[61] M. Jezghani,[21] Z. Ji,[61] J. Jia,[7,60] X. Jiang,[37] B. M. Johnson,[7,21] D. Jouan,[51] D. S. Jumper,[25] S. Kanda,[11] J. H. Kang,[68] D. Kapukchyan,[8] S. Karthas,[61] D. Kawall,[41] A. V. Kazantsev,[34] J. A. Key,[46] V. Khachatryan,[61] A. Khanzadeev,[53] A. Khatiwada,[37] C. Kim,[8,33] D. J. Kim,[31] E.-J. Kim,[30] G. W. Kim,[18] M. Kim,[55,59] B. Kimelman,[43] D. Kincses,[16] E. Kistenev,[7] R. Kitamura,[11] J. Klatsky,[20] D. Kleinjan,[8] P. Kline,[61] T. Koblesky,[12] B. Komkov,[53] D. Kotov,[53,58] S. Kudo,[64] B. Kurgyis,[16] K. Kurita,[57] M. Kurosawa,[55,56] Y. Kwon,[68] R. Lacey,[60] J. G. Lajoie,[28] A. Lebedev,[28] S. Lee,[68] S. H. Lee,[28,61] M. J. Leitch,[37] Y. H. Leung,[61] N. A. Lewis,[42] X. Li,[10] X. Li,[37] S. H. Lim,[12,37,54,68] M. X. Liu,[37] V.-R. Loggins,[25] S. Lökös,[16,17] K. Lovasz,[15] D. Lynch,[7] T. Majoros,[15] Y. I. Makdisi,[6] M. Makek,[69] A. Manion,[61] V. I. Manko,[34] E. Mannel,[7] M. McCumber,[37] P. L. McGaughey,[37] D. McGlinchey,[12,37] C. McKinney,[25] A. Meles,[47] M. Mendoza,[8] W. J. Metzger,[17] A. C. Mignerey,[40] D. E. Mihalik,[61] A. Milov,[66] D. K. Mishra,[4] J. T. Mitchell,[7] Iu. Mitrankov,[58] G. Mitsuka,[32,55,56] S. Miyasaka,[55,63] S. Mizuno,[55,64] A. K. Mohanty,[4] P. Montuenga,[25] T. Moon,[33,68] D. P. Morrison,[7] S. I. Morrow,[65] T. V. Moukhanova,[34] B. Mulilo,[33,55] T. Murakami,[35,55] J. Murata,[55,57] A. Mwai,[60] K. Nagai,[63] K. Nagashima,[22,55] T. Nagashima,[57] J. L. Nagle,[12] M. I. Nagy,[16] I. Nakagawa,[55,56] H. Nakagomi,[55,64] K. Nakano,[55,63] C. Nattrass,[62] S. Nelson,[19] P. K. Netrakanti,[4] T. Niida,[64] S. Nishimura,[11] R. Nishitani,[44] R. Nouicer,[7,56] T. Novák,[17,67] N. Novitzky,[31,61,64] A. S. Nyanin,[34] E. O'Brien,[7] C. A. Ogilvie,[28] J. D. Orjuela Koop,[12] J. D. Osborn,[42] A. Oskarsson,[38] G. J. Ottino,[46] K. Ozawa,[32,64] R. Pak,[7] V. Pantuev,[26] V. Papavassiliou,[47] J. S. Park,[59] S. Park,[55,59,61] S. F. Pate,[47] M. Patel,[28] J.-C. Peng,[25] W. Peng,[65] D. V. Perepelitsa,[7,12] G. D. N. Perera,[47] D. Yu. Peressounko,[34] C. E. PerezLara,[61] J. Perry,[28] R. Petti,[7,61] M. Phipps,[7,25] C. Pinkenburg,[7] R. Pinson,[1] R. P. Pisani,[7] M. Potekhin,[7] A. Pun,[47,49] M. L. Purschke,[7] P. V. Radzevich,[58] J. Rak,[31] N. Ramasubramanian,[61] B. J. Ramson,[42] I. Ravinovich,[66] K. F. Read,[50,62] D. Reynolds,[60] V. Riabov,[45,53] Y. Riabov,[53,58] D. Richford,[5] T. Rinn,[25,28] S. D. Rolnick,[8] M. Rosati,[28] Z. Rowan,[5] J. G. Rubin,[42] J. Runchey,[28] A. S. Safonov,[58] B. Sahlmueller,[61] N. Saito,[32] T. Sakaguchi,[7] H. Sako,[29] V. Samsonov,[45,53] M. Sarsour,[21] S. Sato,[29] C. Y. Scarlett,[19] B. Schaefer,[65] B. K. Schmoll,[62] K. Sedgwick,[8] R. Seidl,[55,56] A. Sen,[28,62] R. Seto,[8] P. Sett,[4] A. Sexton,[40] D. Sharma,[61] I. Shein,[24] T.-A. Shibata,[55,63] K. Shigaki,[22] M. Shimomura,[28,44] T. Shioya,[64] P. Shukla,[4] A. Sickles,[7,25] C. L. Silva,[37] D. Silvermyr,[38,50] B. K. Singh,[3] C. P. Singh,[3] V. Singh,[3] M. J. Skoby,[42] M. Slunečka,[9] K. L. Smith,[20] M. Snowball,[37] R. A. Soltz,[36] W. E. Sondheim,[37] S. P. Sorensen,[62] I. V. Sourikova,[7] P. W. Stankus,[50] M. Stepanov,[41,*] S. P. Stoll,[7] T. Sugitate,[22] A. Sukhanov,[7] T. Sumita,[55] J. Sun,[61] X. Sun,[21] Z. Sun,[15] S. Suzuki,[44] J. Sziklai,[67] A. Taketani,[55,56] K. Tanida,[29,56,59] M. J. Tannenbaum,[7] S. Tarafdar,[65,66] A. Taranenko,[45,60] G. Tarnai,[15] R. Tieulent,[21,39] A. Timilsina,[28] T. Todoroki,[55,56,64] M. Tomášek,[14] C. L. Towell,[1] R. Towell,[1] R. S. Towell,[1] I. Tserruya,[66] Y. Ueda,[22] B. Ujvari,[15] H. W. van Hecke,[37] J. Velkovska,[65] M. Virius,[14] V. Vrba,[14,27] N. Vukman,[69] X. R. Wang,[47,56] Z. Wang,[5] Y. Watanabe,[55,56] Y. S. Watanabe,[11,32] F. Wei,[47] A. S. White,[42] C. P. Wong,[21,37] C. L. Woody,[7] Y. Wu,[8] M. Wysocki,[50] B. Xia,[49] C. Xu,[47] Q. Xu,[65] L. Xue,[21] S. Yalcin,[61] Y. L. Yamaguchi,[11,56,61] H. Yamamoto,[64] A. Yanovich,[24] J. H. Yoo,[33,56] I. Yoon,[59] H. Yu,[47,52] I. E. Yushmanov,[34] W. A. Zajc,[13] A. Zelenski,[6] Y. Zhai,[28] S. Zharko,[58] S. Zhou,[10] and L. Zou[8]

(PHENIX Collaboration)

[1]*Abilene Christian University, Abilene, Texas 79699, USA*

[2]*Department of Physics, Augustana University, Sioux Falls, South Dakota 57197, USA*

[3]*Department of Physics, Banaras Hindu University, Varanasi 221005, India*

[4]*Bhabha Atomic Research Centre, Bombay 400 085, India*

[5]*Baruch College, City University of New York, New York, New York 10010, USA*

[6]*Collider-Accelerator Department, Brookhaven National Laboratory, Upton, New York 11973-5000, USA*

[7]*Physics Department, Brookhaven National Laboratory, Upton, New York 11973-5000, USA*

[8]*University of California-Riverside, Riverside, California 92521, USA*

[9]*Charles University, Ovocný trh 5, Praha 1, 116 36, Prague, Czech Republic*
[10]*Science and Technology on Nuclear Data Laboratory, China Institute of Atomic Energy, Beijing 102413, People's Republic of China*
[11]*Center for Nuclear Study, Graduate School of Science, University of Tokyo, 7-3-1 Hongo, Bunkyo, Tokyo 113-0033, Japan*
[12]*University of Colorado, Boulder, Colorado 80309, USA*
[13]*Columbia University, New York, New York 10027 and Nevis Laboratories, Irvington, New York 10533, USA*
[14]*Czech Technical University, Zikova 4, 166 36 Prague 6, Czech Republic*
[15]*Debrecen University, H-4010 Debrecen, Egyetem tér 1, Hungary*
[16]*ELTE, Eötvös Loránd University, H-1117 Budapest, Pázmány P. s. 1/A, Hungary*
[17]*Eszterházy Károly University, Károly Róbert Campus, H-3200 Gyöngyös, Mátrai út 36, Hungary*
[18]*Ewha Womans University, Seoul 120-750, Korea*
[19]*Florida A&M University, Tallahassee, Florida 32307, USA*
[20]*Florida State University, Tallahassee, Florida 32306, USA*
[21]*Georgia State University, Atlanta, Georgia 30303, USA*
[22]*Hiroshima University, Kagamiyama, Higashi-Hiroshima 739-8526, Japan*
[23]*Department of Physics and Astronomy, Howard University, Washington, DC 20059, USA*
[24]*IHEP Protvino, State Research Center of Russian Federation, Institute for High Energy Physics, Protvino, 142281, Russia*
[25]*University of Illinois at Urbana-Champaign, Urbana, Illinois 61801, USA*
[26]*Institute for Nuclear Research of the Russian Academy of Sciences, prospekt 60-letiya Oktyabrya 7a, Moscow 117312, Russia*
[27]*Institute of Physics, Academy of Sciences of the Czech Republic, Na Slovance 2, 182 21 Prague 8, Czech Republic*
[28]*Iowa State University, Ames, Iowa 50011, USA*
[29]*Advanced Science Research Center, Japan Atomic Energy Agency, 2-4 Shirakata Shirane, Tokai-mura, Naka-gun, Ibaraki-ken 319-1195, Japan*
[30]*Jeonbuk National University, Jeonju, 54896, Korea*
[31]*Helsinki Institute of Physics and University of Jyväskylä, P.O. Box 35, FI-40014 Jyväskylä, Finland*
[32]*KEK, High Energy Accelerator Research Organization, Tsukuba, Ibaraki 305-0801, Japan*
[33]*Korea University, Seoul 02841, Korea*
[34]*National Research Center "Kurchatov Institute", Moscow, 123098 Russia*
[35]*Kyoto University, Kyoto 606-8502, Japan*
[36]*Lawrence Livermore National Laboratory, Livermore, California 94550, USA*
[37]*Los Alamos National Laboratory, Los Alamos, New Mexico 87545, USA*
[38]*Department of Physics, Lund University, Box 118, SE-221 00 Lund, Sweden*
[39]*IPNL, CNRS/IN2P3, Univ Lyon, Université Lyon 1, F-69622, Villeurbanne, France*
[40]*University of Maryland, College Park, Maryland 20742, USA*
[41]*Department of Physics, University of Massachusetts, Amherst, Massachusetts 01003-9337, USA*
[42]*Department of Physics, University of Michigan, Ann Arbor, Michigan 48109-1040, USA*
[43]*Muhlenberg College, Allentown, Pennsylvania 18104-5586, USA*
[44]*Nara Women's University, Kita-uoya Nishi-machi Nara 630-8506, Japan*
[45]*National Research Nuclear University, MEPhI, Moscow Engineering Physics Institute, Moscow, 115409, Russia*
[46]*University of New Mexico, Albuquerque, New Mexico 87131, USA*
[47]*New Mexico State University, Las Cruces, New Mexico 88003, USA*
[48]*Physics and Astronomy Department, University of North Carolina at Greensboro, Greensboro, North Carolina 27412, USA*
[49]*Department of Physics and Astronomy, Ohio University, Athens, Ohio 45701, USA*
[50]*Oak Ridge National Laboratory, Oak Ridge, Tennessee 37831, USA*
[51]*IPN-Orsay, Université Paris-Sud, CNRS/IN2P3, Université Paris-Saclay, BP1, F-91406, Orsay, France*
[52]*Peking University, Beijing 100871, People's Republic of China*
[53]*PNPI, Petersburg Nuclear Physics Institute, Gatchina, Leningrad region, 188300, Russia*
[54]*Pusan National University, Busan, 46241, South Korea*
[55]*RIKEN Nishina Center for Accelerator-Based Science, Wako, Saitama 351-0198, Japan*
[56]*RIKEN BNL Research Center, Brookhaven National Laboratory, Upton, New York 11973-5000, USA*
[57]*Physics Department, Rikkyo University, 3-34-1 Nishi-Ikebukuro, Toshima, Tokyo 171-8501, Japan*
[58]*Saint Petersburg State Polytechnic University, St. Petersburg 195251, Russia*
[59]*Department of Physics and Astronomy, Seoul National University, Seoul 151-742, Korea*
[60]*Chemistry Department, Stony Brook University, SUNY, Stony Brook, New York 11794-3400, USA*
[61]*Department of Physics and Astronomy, Stony Brook University, SUNY, Stony Brook, New York 11794-3800, USA*
[62]*University of Tennessee, Knoxville, Tennessee 37996, USA*
[63]*Department of Physics, Tokyo Institute of Technology, Oh-okayama, Meguro, Tokyo 152-8551, Japan*
[64]*Tomonaga Center for the History of the Universe, University of Tsukuba, Tsukuba, Ibaraki 305, Japan*
[65]*Vanderbilt University, Nashville, Tennessee 37235, USA*
[66]*Weizmann Institute, Rehovot 76100, Israel*

[67]*Institute for Particle and Nuclear Physics, Wigner Research Centre for Physics, Hungarian Academy of Sciences (Wigner RCP, RMKI) H-1525 Budapest 114, PO Box 49, Budapest, Hungary*
[68]*Yonsei University, IPAP, Seoul 120-749, Korea*
[69]*Department of Physics, Faculty of Science, University of Zagreb, Bijenička c. 32 HR-10002 Zagreb, Croatia*

(Received 5 November 2019; revised 30 March 2020; accepted 26 May 2020; published 6 July 2020)

Charmonium is a valuable probe in heavy-ion collisions to study the properties of the quark gluon plasma, and is also an interesting probe in small collision systems to study cold nuclear matter effects, which are also present in large collision systems. With the recent observations of collective behavior of produced particles in small system collisions, measurements of the modification of charmonium in small systems have become increasingly relevant. We present the results of J/ψ measurements at forward and backward rapidity in various small collision systems, $p+p$, $p+$Al, $p+$Au, and ^{3}He$+$Au, at $\sqrt{s_{NN}} = 200$ GeV. The results are presented in the form of the observable R_{AB}, the nuclear modification factor, a measure of the ratio of the J/ψ invariant yield compared to the scaled yield in $p+p$ collisions. We examine the rapidity, transverse momentum, and collision centrality dependence of nuclear effects on J/ψ production with different projectile sizes p and ^{3}He, and different target sizes Al and Au. The modification is found to be strongly dependent on the target size, but to be very similar for $p+$Au and ^{3}He$+$Au. However, for 0%–20% central collisions at backward rapidity, the modification factor for ^{3}He$+$Au is found to be smaller than that for $p+$Au, with a mean fit to the ratio of $0.89 \pm 0.03(\text{stat}) \pm 0.08(\text{syst})$, possibly indicating final state effects due to the larger projectile size.

DOI: 10.1103/PhysRevC.102.014902

I. INTRODUCTION

The cross section for production of charmonium in proton collisions with heavy nuclei is strongly modified relative to that in $p+p$ collisions. The effects that cause this modification are often referred to as cold nuclear matter (CNM) effects because of the longstanding presumption that the energy density and temperature produced in the collision of a single proton with a nucleus were not sufficient to form a deconfined quark-gluon plasma, as produced in ultrarelativistic heavy ion collisions at the BNL Relativistic Heavy Ion Collider (RHIC) and the CERN Large Hadron Collider (LHC). A major motivation for this work is to study CNM effects that can modify charm production in $p+A$ collisions, which include modification of the nuclear-parton-distribution functions (nPDFs) in a nucleus [1,2], initial state parton energy loss [3], breakup of the forming charmonium in collisions with target nucleons [4,5], coherent gluon saturation [6,7], and transverse momentum broadening [8]. These mechanisms are generally expected to act in the early stages of the collision, and effect either the production rates of charm quarks or their propagation through the nucleus. All of these processes are strongly (and differently) dependent on the rapidity and transverse momentum of the produced charmonium, and the collision energy. They are therefore best studied using $p+A$ data covering the broadest possible range of collision energy, rapidity and transverse momentum.

At RHIC, $p+p$, $d+$Au, $p+$Au, ^{3}He$+$Au and $p+$Al collisions have been studied at $\sqrt{s_{NN}} = 200$ GeV. The PHENIX experiment published data on J/ψ production in $d+$Au collisions over the rapidity intervals $1.2 < |y| < 2.2$ and $|y| < 0.35$ [9,10]. PHENIX also reported measurements of the $\psi(2S)$ in small collision systems, first with nuclear modification in $d+$Au collisions ($|y| < 0.35$) [11], followed by measurements of the ratio of $\psi(2S)$ to J/ψ in $p+$Al, $p+$Au and ^{3}He$+$Au collisions at $\sqrt{s_{NN}} = 200$ GeV ($1.2 < |y| < 2.2$) [12]. The STAR collaboration has reported J/ψ nuclear modification data for $d+$Au collisions ($|y| < 1$) [13].

At the LHC, nuclear effects in $p+$Pb collisions have been studied at $\sqrt{s_{NN}} = 5.02$ TeV. The ALICE collaboration has reported data for J/ψ [14,15] and $\psi(2S)$ [16,17] ($-4.46 < y < -2.96$ and $2.03 < y < 3.53$). The LHCb collaboration has reported J/ψ [18] and $\psi(2S)$ data [19] ($-5.0 < y < -2.5$ and $1.5 < y < 4.0$). The CMS collaboration has reported J/ψ [20] and $\psi(2S)$ [21] data ($-2.4 < y < 1.93$ and $p_T > 4\,\text{GeV}/c$). The ATLAS collaboration has reported J/ψ [22] and charmonium [23] data ($|y| < 2$ and $p_T > 8\,\text{GeV}/c$). These measurements show a significant energy, rapidity, and p_T dependence of the modification of charmonia production compared to the scaled $p+p$ results.

The assumption that effects due to soft particles produced in the collision are not important in p or $d+A$ collision at colliders was called into question by the observation of strong suppression of the $\psi(2S)$ relative to the J/ψ in central $d+$Au collisions [11], and then in $p+$Pb collisions [16]. Because CNM effects on the production of charm quarks and their transport through the nucleus are expected to affect both states similarly, they do not appear to be able to explain this

*Deceased.
†PHENIX Spokesperson: akiba@rcf.rhic.bnl.gov

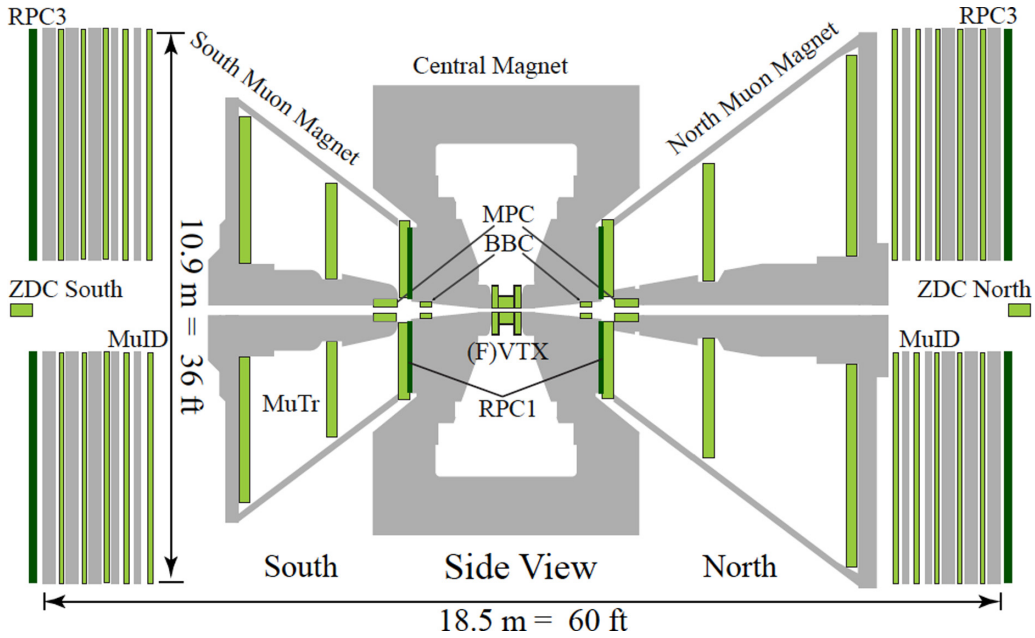

FIG. 1. Side view of the PHENIX detector in 2014 and 2015.

observation. However, it can be reproduced by the co-mover break up model [24], where charmonium is dissociated by interactions with produced particles in the final state, which naturally gives a larger suppression effect on the much more weakly bound $\psi(2S)$. The observation of flow-like behavior in $p+$Pb collisions at LHC (see for example [25]) and later in $d+$Au collisions at RHIC [26,27] suggested that a quark-gluon plasma of small size may be formed in high energy collisions of these light systems. This led to the application of transport models to $p+$Pb and $d+$Au data, which were originally developed for charmonium production in heavy ion collisions [28,29]. A plasma phase in these small collision systems gives different suppression between the charmonia states and allows a description of the data. In the case of most central midrapidity $d+$Au collisions at $\sqrt{s_{NN}} = 200$ GeV, additional suppression beyond CNM effects has been predicted of approximately 20% for the J/ψ, and 55% for the $\psi(2S)$ [28], in good agreement with the data [9,11].

In 2014 and 2015, RHIC provided collisions of $p+$Al, $p+$Au, and ^{3}He +Au for a systematic study of small systems. A comparison of flow data from $p+$Au, $d+$Au, and ^{3}He +Au with hydrodynamic models found that the data were all consistent with hydrodynamic flow in the most central collisions [30–32]. An obvious question is whether increased energy density provided by the ^{3}He projectile in comparison to the proton produces any observable effect on charmonium modification in collisions with a Au target.

In this paper we present PHENIX measurements of inclusive J/ψ production in $p+$Al, $p+$Au, and ^{3}He +Au collisions at $\sqrt{s_{NN}} = 200$ GeV. The inclusive J/ψ cross section includes feed-down from $\psi(2S)$ and χ_c states, and a smaller contribution from B-meson decays. The results are directly compared to $p+p$ collisions at the same center of mass energy by calculating the nuclear modification factor R_{AB}. The J/ψ data are presented as a function of p_T, rapidity, and centrality and are compared to theoretical models.

II. EXPERIMENTAL SETUP

The PHENIX detector [33] comprises two central arm spectrometers at midrapidity and two muon arm spectrometers at forward and backward rapidity. The detector configuration during the data taking in 2014 and 2015 is shown in Fig. 1. The data presented here are from $J/\psi \to \mu^+\mu^-$ decays recorded with the muon arm spectrometers. The muon spectrometers have full azimuthal acceptance, covering $-2.2 < \eta < -1.2$ (south arm) and $1.2 < \eta < 2.4$ (north arm), where the forward arm has a slightly larger acceptance than the backward arm. For dimuons, the analysis is restricted to $1.2 < |y| < 2.2$ in both arms. Each muon arm comprises a forward silicon vertex tracker (FVTX), followed by a hadron absorber and a muon spectrometer.

The FVTX [34] is a silicon detector designed to measure a precise collision vertex [also constrained by the silicon vertex tracker (VTX) at midrapidity], and to provide precise tracking for charged particles entering the muon spectrometer before undergoing multiple scattering in the hadron absorber. The FVTX was not used in this inclusive J/ψ analysis, because the acceptance is reduced when requiring muon arm tracks that match tracks in the FVTX. Following the FVTX is the hadron absorber, composed of layers of copper, iron, and stainless steel, corresponding to 7.2 nuclear interaction lengths (λ_I). The absorber suppresses hadrons in front of the muon arm by a factor of approximately 1000, thus significantly reducing hadronic background for muon based measurements.

Each of the muon spectrometers is composed of a muon tracker (MuTr) embedded in a magnetic field followed by a muon identifier (MuID). Each MuTr comprises three stations

of cathode strip chambers, inside a magnet with a radial field integral of $\int \mathrm{B} \cdot dl = 0.72$ T m. It provides a momentum measurement for charged particles. Each MuID is composed of five layers (referred to as gap 0–4) of steel absorber [4.8 (5.4) λ_I for south (north) arm] and two planes of Iarocci tubes. This enables the separation of muons and hadrons based on their penetration depth at a given reconstructed momentum. The MuID in each arm is also used to trigger events containing two or more muon tracks per event, called a dimuon trigger, and each muon track is required to have at least one hit in either gap 3 or gap 4. A more detailed discussion of the PHENIX muon arms can be found in Refs. [35,36].

The beam-beam counters (BBC) are used to determine the collision vertex position along the beam axis (z_{BBC}) with a resolution of roughly 2 cm in $p+p$ collisions. Each BBC comprises two arrays of 64 quartz Čerenkov detectors located at $z = \pm 144$ cm from the nominal interaction point, and has an acceptance covering the full azimuth and $3.1 < |y| < 3.9$. They also provide a minimum bias (MB) trigger by requiring at least one hit in each BBC. The BBC trigger efficiency, determined from the Van der Meer scan technique [37], is $55\% \pm 5\%$ for inelastic $p+p$ events and $79\% \pm 2\%$ for events with midrapidity particle production [38,39]. In $p+$Al, $p+$Au, and ^{3}He$+$Au collisions, charged particle multiplicity in the BBC in the Au/Al-going direction ($-3.9 < y < -3.1$) is used to categorize the event centrality. The BBC trigger efficiency is $72\% \pm 4\%$, $84\% \pm 3\%$, and $88\% \pm 4\%$ of inelastic $p+$Al, $p+$Au, and ^{3}He$+$Au collisions, respectively.

A Glauber model, combined with a simulation of the BBC response, is used to relate charged particle multiplicity in the BBC to parameters that characterize the collision centrality, as described in [39]. The analysis produces the average number of nucleon-nucleon collisions in each centrality category. It also produces centrality dependent BBC bias correction factors which account for the correlation between BBC charge and the presence of a hard scattering in the event, and are applied as a multiplicative correction on invariant yields. Table I shows the values of $\langle N_{\mathrm{coll}} \rangle$ and BBC bias correction factor from this analysis.

TABLE I. $\langle N_{\mathrm{coll}} \rangle$ and BBC bias correction factors for different centrality bins of p+Al, p+Au and ^{3}He$+$Au collisions.

Collision system	Centrality	$\langle N_{\mathrm{coll}} \rangle$	Bias factor
p+Al	0%–20%	3.4 ± 0.3	0.81 ± 0.01
	20%–40%	2.4 ± 0.1	0.90 ± 0.02
	40%–72%	1.7 ± 0.1	1.04 ± 0.04
	0%–100%	2.1 ± 0.1	0.80 ± 0.02
p+Au	0%–5%	9.7 ± 0.6	0.86 ± 0.01
	5%–10%	8.4 ± 0.6	0.90 ± 0.01
	10%–20%	7.4 ± 0.5	0.94 ± 0.01
	0%–20%	8.2 ± 0.5	0.90 ± 0.01
	20%–40%	6.1 ± 0.4	0.98 ± 0.01
	40%–60%	4.4 ± 0.3	1.03 ± 0.01
	60%–84%	2.6 ± 0.2	1.00 ± 0.06
	0%–100%	4.7 ± 0.3	0.86 ± 0.01
^{3}He$+$Au	0%–20%	22.3 ± 1.7	0.95 ± 0.01
	20%–40%	14.8 ± 1.1	0.95 ± 0.01
	40%–88%	5.5 ± 0.4	1.03 ± 0.01
	0%–100%	10.4 ± 0.7	0.89 ± 0.01

III. DATA ANALYSIS

A. Data set

The data sets used in this analysis are ^{3}He$+$Au data collected in 2014, and $p+p$, $p+$Al, and $p+$Au data collected in 2015. All data sets were recorded at a center of mass energy $\sqrt{s_{NN}} = 200$ GeV. The events considered here are triggered by the dimuon trigger and are required to have a vertex within ± 30 cm of the center of the interaction region. The corresponding integrated luminosity is 47 pb^{-1} for $p+p$, 590 nb^{-1} for $p+$Al, 138 nb^{-1} for $p+$Au, and 18 nb^{-1} for ^{3}He$+$Au collisions.

B. J/ψ signal extraction

Yields of J/ψ mesons were extracted from the invariant mass spectra constructed from combinations of unlike-sign tracks that are identified as muons (see Fig. 2). The mass

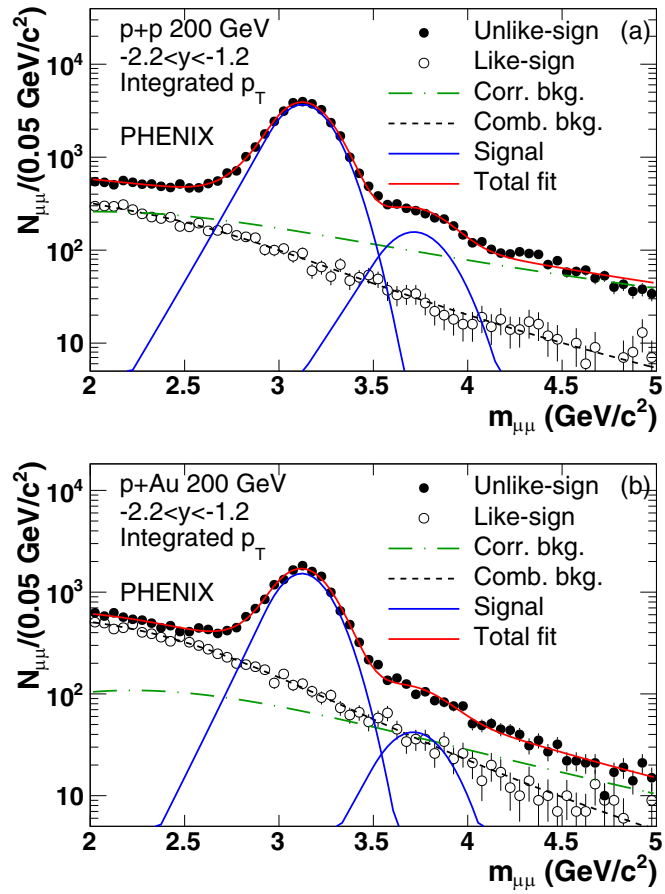

FIG. 2. Invariant mass distributions of unlike-sign and like-sign dimuons in $p+p$ and integrated centrality of $p+$Au collisions in the south muon arm. Fit results to extract the J/ψ signal are also presented.

spectra contain muon pairs from J/ψ decays, as well as significant contributions from combinations of real muons not from a J/ψ, as well as misidentified hadrons. Details about the dimuon selection to reduce the background contributions are described in [40,41].

The mass spectrum constructed from like-sign tracks was used to estimate the background due to random combinations of kinematically unrelated tracks. A modified Hagedorn function was used to represent the correlated background due to kinematically related tracks. For J/ψ signal extraction, crystal-ball functions [42] were used to describe the J/ψ and $\psi(2S)$ peaks, similar to the previous analysis in small collision systems [12]:

$$f(m) = N\exp\left(-\frac{(m-\bar{m})^2}{2\sigma^2}\right), \quad \text{for} \quad \frac{m-\bar{m}}{\sigma} > -\alpha,$$
$$f(m) = NA\left(B - \frac{(m-\bar{m})^2}{\sigma}\right)^{-n}, \quad \text{for} \quad \frac{m-\bar{m}}{\sigma} \leqslant -\alpha, \quad (1)$$
$$A = \left(\frac{n}{|\alpha|}\right)^n \exp\left(-\frac{|\alpha|^2}{2}\right), \quad B = \frac{n}{|\alpha|} - |\alpha|,$$

where σ and $\bar{m}$ are the width and mass centroid of the Gaussian component of the line shape and α and n are parameters describing the tail.

The crystal-ball shape and tail parameters for the $\psi(2S)$ were fixed with respect to the J/ψ parameters, using the PDG database value [43] for the energy difference and a width broadening factor taken from simulations. In cases where the statistical precision of the data led to poor definition of the J/ψ signal shape, the mass and width of the J/ψ peak were fixed and a systematic uncertainty was assigned to the yield based on tests made with higher statistics cases. The statistical uncertainties related to the extraction of the J/ψ yields were determined from a covariance matrix in the fitting procedure.

C. Background estimation

The random combinatorial background in the unlike-sign mass spectrum was approximated by combining all like-sign tracks from the same events. There is a small correlated contribution to the like-sign pairs from jets and open bottom; however, compared to the other background sources, this is small.

The correlated background comprises unlike-sign muon pairs from charm, bottom, jets, and Drell-Yan. Because the correlated background cannot be estimated independently from the data, it must be fitted to the mass spectrum when the J/ψ yield is extracted. Fitting the correlated background effectively compensates for the small correlated component included in the like-sign estimation of the combinatorial background.

We describe the correlated background using a modified Hagedorn function [40,44,45]:

$$\frac{d^2N}{dm_{\mu\mu}dp_T} = \frac{p_0}{\left[\exp\left(-p_1 m_{\mu\mu} - p_2 m_{\mu\mu}^2\right) + m_{\mu\mu}/p_3\right]^{p_4}}, \quad (2)$$

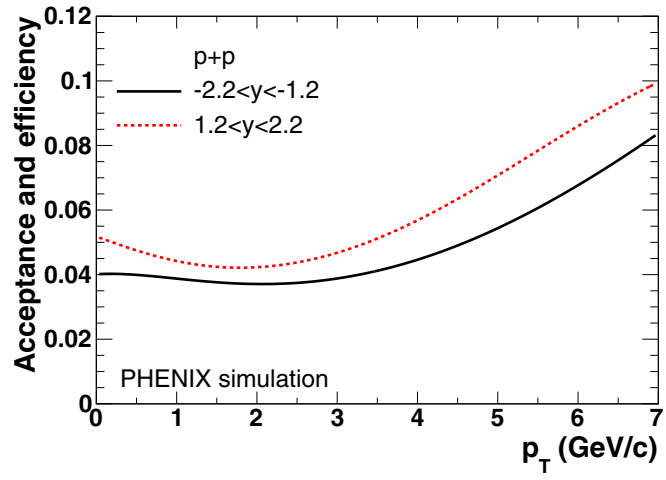

FIG. 3. Acceptance and reconstruction efficiency as a function of p_T for dimuons from J/ψ decays in $p+p$ collisions. GEANT4 simulations evaluate detector acceptance×efficiency simultaneously.

where $m_{\mu\mu}$ is the reconstructed J/ψ mass, p_0 is a normalization parameter, p_4 is the high mass tail parameter, and p_1, p_2, and p_3 are additional fit parameters. It was found during the analysis that when fitting mass spectra with poor statistical precision, the shape of the correlated background was not well defined. This led to a contribution of less than 10% to the point-to-point uncertainty in the J/ψ yields. Therefore, the shape of the correlated background as a function of p_T (determined by p_1, p_2, and p_3) was constrained using simulation results based on a detailed study of dimuon mass spectra [9,40,46,47]. A systematic uncertainty on the J/ψ yield was assigned for this procedure by refitting the data with various combinations of correlated background parameters left free.

D. Efficiency correction

1. Acceptance and reconstruction efficiency

The study of acceptance and reconstruction efficiency of dimuons from J/ψ decays has been performed using a GEANT4-based full detector simulation [48]. In this simulation, the MuTr and MuID detector efficiencies are set to values determined from the data. An emulator of the dimuon trigger response is included in the simulation to account for the trigger efficiency. As these efficiencies depend on the instantaneous luminosity being sampled, each data set is divided into three groups with different beam interaction rates, and corrected yields with separate corrections are compared. A systematic uncertainty is assigned to the extracted J/ψ cross sections times branching fraction to $\mu^+\mu^-$ to reflect the differences, see Sec. III G for details.

The PYTHIA8 event generator package [49] is utilized to generate J/ψ events used for the full GEANT4 detector simulation. To take into account effects from background hits, the simulated hits of PYTHIA8 J/ψ events are embedded into real data events, separated into centrality classes of the collision system. The track reconstruction is then run on the data with embedded simulated hits to examine the effects of the underlying event on the reconstruction efficiency. Figure 3 shows

the acceptance and reconstruction efficiency for the J/ψ as a function of p_T in $p+p$ collisions. The difference between the two muon arms is mainly from different inefficient detector areas. There is little multiplicity effect on the reconstruction efficiency in small collision systems, the relative difference between 0%–20% and 40%–88% centrality bins at backward rapidity in ^{3}He +Au collisions is about 5%.

E. Invariant yield and nuclear modification factor

The invariant yield of dimuons from J/ψ decays in a given rapidity and centrality bin for the integrated p_T range is

$$B_{ll}\frac{dN}{dy} = \frac{1}{\Delta y}\frac{c_{\rm BBC}}{\varepsilon_{\rm Ae}\varepsilon_{\rm trig}}\frac{N_{J/\psi}}{N_{\rm evt}}, \tag{3}$$

where B_{ll} is the branching ratio of J/ψ to dimuons, Δy is the width of the rapidity bin, $N_{J/\psi}$ is the number of J/ψ obtained from the fit procedure, $c_{\rm BBC}$ is the BBC bias correction factor described in Table I, $N_{\rm evt}$ is the number of sampled MB events in the given centrality bin, $\varepsilon_{\rm Ae}$ is the J/ψ acceptance and reconstruction efficiency, and $\varepsilon_{\rm trig}$ is the dimuon trigger efficiency.

The invariant yield in a y, p_T, and centrality bin is

$$\frac{B_{ll}}{2\pi p_T}\frac{d^2N}{dy dp_T} = \frac{1}{2\pi p_T \Delta p_T \Delta y}\frac{c_{\rm BBC}}{\varepsilon_{\rm Ae}\varepsilon_{\rm trig}}\frac{N_{J/\psi}}{N_{\rm evt}}, \tag{4}$$

where Δp_T is the width of the p_T bin, and in this case $N_{\rm evt}$ is the number of events in the centrality bin. Based on the invariant yields calculated with Eq. (4), the J/ψ nuclear modification factor R_{AB} for a given y, p_T, and centrality bin is formed to quantify nuclear effects in $p+$Al, $p+$Au, and ^{3}He +Au collisions. The R_{AB} is defined as

$$R_{AB} = \frac{1}{\langle N_{\rm coll}\rangle}\frac{d^2N^{AB}/dy dp_T}{d^2N^{pp}/dy dp_T}, \tag{5}$$

where $d^2N^{AB}/dy dp_T$ is the J/ψ invariant yield for a certain centrality bin of $A+B$ collisions, $d^2N^{pp}/dy dp_T$ is the corresponding J/ψ invariant yield for $p+p$ collisions, and $\langle N_{\rm coll}\rangle$ is the mean number of binary collisions for that centrality bin in $A+B$ collisions.

F. $\langle p_T^2\rangle$ calculation

The $\langle p_T^2\rangle$ values for various centrality bins in all collision systems have been calculated over the full measured p_T range ($0 < p_T < 7$ GeV/c). We do not extrapolate the p_T distribution beyond 7 GeV/c. A previous study [10] determined that extrapolating to infinite p_T increased the $\langle p_T^2\rangle$ values by 3%. The value of $\langle p_T^2\rangle$ is calculated numerically using the following formula:

$$\langle p_T^2\rangle = \frac{\sum_{i=0}^{N} p_{T,i}^2 w_i}{\sum_{i=0}^{N} w_i}, \tag{6}$$

where $p_{T,i}$ is the center of the ith p_T bin, and w_i is the weight factor proportional to the J/ψ invariant yield in the p_T bin

$$w_i = p_{T,i} dp_{T,i}\left(\frac{B_{ll}}{2\pi p_T}\frac{d^2N}{dy dp_T}\right)_i, \tag{7}$$

where $dp_{T,i}$ is the width of the bin.

TABLE II. Fractional systematic uncertainties on the signal extraction in $p+p$, $p+$Al, $p+$Au, and ^{3}He +Au collisions at forward (north arm) and backward (south arm) rapidity.

System	Source	Forward	Backward	Type
$p+p$	Corr. bkg.	1.4%	1.8%	B
$p+$Al		1.4%	1.8%	B
$p+$Au		1.9%–2.7%	1.4%–2.8%	B
^{3}He +Au		2.3%–2.4%	1.4%–2.8%	B
$p+p$	Comb. bkg.	<1.0%	<1.0%	B
$p+$Al		1.0%	4.4%	B
$p+$Au		1.0%	1.0%	B
^{3}He +Au		1.0%	2.7%	B
$p+p$	Signal shape	–	–	B
$p+$Al		1.1%	1.1%	B
$p+$Au		0%–1.5%	0%–2.9%	B
^{3}He +Au		1.5%	2.9%	B

G. Systematic uncertainties

In the measurements we present in the next section, Type A uncertainties are uncorrelated point to point uncertainties, and are dominated by the statistical precision of the data. Type B systematic uncertainties are correlated point to point uncertainties. Type C global uncertainties are fractional uncertainties that apply to all measurements uniformly.

1. Signal extraction

As discussed in Sec. III C, the modified Hagedorn function in Eq. (2) was used to describe the correlated background. Initial parameters were estimated based on the previous measurement of dimuon mass spectra [40,46], and two parameters, p_0 and p_4, were left free to describe dimuon mass distributions in the data more properly. For the systematic uncertainty study, additional parameters, p_1, p_2, and p_3, in the modified Hagedorn function were also freed in the fit procedure. We observe 1.4%–2.8% variations of J/ψ counts depending on rapidity, p_T, and centrality.

To describe the combinatorial background shape, the modified Hagedorn function in Eq. (2), used for the correlated background component, was also used to fit like-sign dimuon mass distributions. The effect of statistical fluctuations in the like-sign dimuon mass distributions was studied by varying the shape based on the statistical uncertainties of the fit parameters. We observe 1.0%–4.4% variations of J/ψ counts depending on rapidity, p_T, and centrality.

The uncertainty related to fixing the J/ψ mass centroid and width was evaluated by directly comparing the difference in yields with the parameters free versus fixed, which ranges from 1.1%–2.9% uncertainty.

Table II lists all Type B uncertainties arising from the J/ψ signal extraction.

2. Acceptance and efficiency correction

The acceptance and reconstruction efficiency correction and trigger efficiency correction are obtained from simulation, so discrepancies between the data and calculations can be a source of systematic uncertainty. The discrepancies can be

due to a variation in the detector performance during the data taking period and/or inaccuracy of detector geometry and dead channel maps in the simulation. To quantify these effects, we divide each data set into three groups of different detector efficiency, based on the beam instantaneous luminosity and calculated invariant yields with separate correction factors. In this comparison we observe 1.5%–5.0% variations, depending on rapidity and data set, and assign this variation as a systematic uncertainty. In addition, we compare the azimuthal angle ϕ distribution of tracks in the MuTr between the data and simulation, and assign a 2.5%–6.0% systematic uncertainty depending on rapidity and data set.

In the simulation procedure, PYTHIA8 was used to generate J/ψ events, and initial J/ψ rapidity and p_T shapes in PYTHIA8 are tuned to match the measurements in $p+p$ and $d+\mathrm{Au}$ collisions [9,10,41]. These two different assumptions of the distributions are used as bounds to estimate the sensitivity of this analysis to the shapes of these distributions in $p+\mathrm{Al}$, $p+\mathrm{Au}$, and ^{3}He +Au collisions, which are not known *a priori*. The variation of acceptance and reconstruction efficiency between two sets of rapidity and p_T distributions is less than 2%, so we assigned a 2% conservative systematic uncertainty.

The uncertainty in the dimuon acceptance caused by lack of knowledge of the J/ψ polarization was studied as described in [41]. Because there is no precise measurement of J/ψ polarization, a maximum polarization value (± 1 in the helicity frame) was considered to study the systematic uncertainty. The variation of dimuon acceptance becomes larger as J/ψ p_T decreases, and 9%–20% systematic uncertainties are assigned depending on p_T. We assumed that the J/ψ polarization is not significantly modified in $p+\mathrm{Al}$, $p+\mathrm{Au}$, and ^{3}He +Au collisions, and this uncertainty is canceled in the R_{AB} calculation. This assumption was also made in a similar PHENIX analysis for J/ψ nuclear modification in $d+\mathrm{Au}$ collisions [10].

To evaluate a systematic uncertainty on the dimuon trigger efficiency, the single muon trigger efficiency in the MB triggered data obtained with a large number of muon samples was compared with the emulated single muon trigger efficiency determined from simulation. This difference was propagated to the uncertainty in the dimuon trigger efficiency based on a previous study [40], and a 1.0%–4.8% systematic uncertainty was assigned. The Type B systematic uncertainties related to acceptance and efficiency correction are shown in Table III.

3. Multiple interaction

Due to the high instantaneous beam luminosity, particularly in $p+p$ and $p+\mathrm{Al}$ runs, it is possible to have multiple inelastic collisions from a single beam crossing, which can affect the invariant yield calculation. To investigate this effect, the variation among invariant yields in three groups of different instantaneous luminosity for each data set was studied, revealing a yield variation smaller than 5%. However, the instantaneous luminosity dependence of the acceptance and efficiency correction is already included as a systematic uncertainty, and so no additional systematic uncertainty is assigned.

TABLE III. Fractional systematic uncertainties on the acceptance and efficiency correction in $p+p$, $p+\mathrm{Al}$, $p+\mathrm{Au}$ and ^{3}He +Au collisions at forward (north arm) and backward (south arm) rapidity.

System	Source	Forward	Backward	Type
$p+p$	Run variation	4.0%	4.7%	B
$p+\mathrm{Al}$		2.8%	3.3%	B
$p+\mathrm{Au}$		1.6%	3.5%	B
^{3}He +Au		1.5%	5.0%	B
$p+p$	ϕ matching	5.8%	5.0%	B
$p+\mathrm{Al}$		3.6%	3.3%	B
$p+\mathrm{Au}$		3.4%	4.0%	B
^{3}He +Au		3.1%	2.5%	B
all	Initial shape	2.0%	2.0%	B
all	J/ψ pol.	10%–20%	9%–20%	B
$p+p$	Trigger eff.	1.0%–1.7%	1.0%–2.6%	B
$p+\mathrm{Al}$		1.0%–1.8%	2.0%–4.6%	B
$p+\mathrm{Au}$		1.0%–1.7%	1.0%–4.8%	B
^{3}He +Au		1.0%–2.4%	1.0%–2.4%	B

4. $\langle p_T^2 \rangle$

The $\langle p_T^2 \rangle$ uncertainty is calculated based on the systematic uncertainty of the invariant yield as a function of p_T. The systematic uncertainties are mostly point-to-point correlated, and we assumed that the uncertainties in different p_T bins are linearly correlated. The upper and lower limits of invariant yield in each p_T bin are taken to calculate the upper and lower limits of $\langle p_T^2 \rangle$.

5. $\langle N_{\mathrm{coll}} \rangle$ and BBC efficiency

The systematic uncertainties on the BBC efficiency and the determination of $\langle N_{\mathrm{coll}} \rangle$ in $p+\mathrm{Al}$, $p+\mathrm{Au}$, and ^{3}He +Au collisions described in Table I are evaluated by following the procedure developed in the previous PHENIX analyses of $d+\mathrm{Au}$ data [39]. These systematic uncertainties are considered as Type C (Type B) systematic uncertainties in rapidity and p_T (centrality) dependence results. The systematic uncertainty on the BBC efficiency in $p+p$ collisions obtained in [38] is 10.1%, and this systematic uncertainty is considered as a Type C systematic uncertainty.

IV. RESULTS

In this section, we present invariant yield, nuclear modification factor, and $\langle p_T^2 \rangle$ results at forward and backward rapidity. There have been significant changes to the muon arm configuration and to the simulation framework since the $d+\mathrm{Au}$ data set was recorded. Figure 4 shows the J/ψ invariant yield as a function of p_T in $p+p$ collisions at $\sqrt{s} = 200$ GeV at forward and backward rapidity, where bars (boxes) represent point-to-point uncorrelated (correlated) uncertainties. The global systematic uncertainty is 10.1%. The ratio of invariant yields between the forward and backward rapidity regions is presented in the bottom panel, where the systematic uncertainty due to the J/ψ polarization cancels in the ratio. The invariant yields at forward and backward rapidity are consistent within the systematic uncertainties,

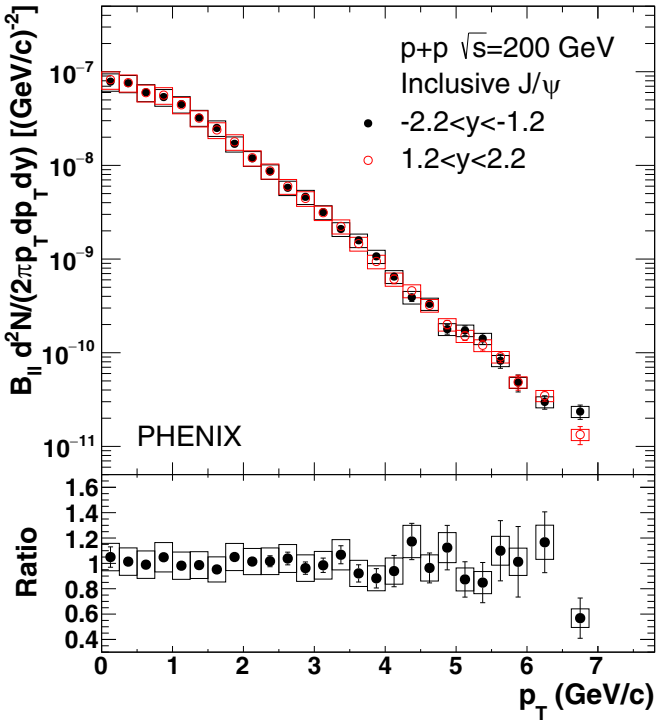

FIG. 4. J/ψ invariant yields as a function of p_T in $p+p$ collisions at $\sqrt{s} = 200$ GeV. The ratio between the values for the two muon arms is presented in the bottom panel. Bars (boxes) around data points represent point-to-point uncorrelated (correlated) uncertainties. There is also a global systematic uncertainty of 10.1%

confirming that the detector efficiency is well understood in $p+p$ collisions.

Plots and tables of invariant yield are presented for the other collision systems in the Appendix. We focus here on the nuclear modification factors.

Figure 5 shows the rapidity dependence of the nuclear modification factor for 0%–100% centrality in $p+$Al, $p+$Au, and ^{3}He +Au collisions. The rapidity dependence of the nuclear modification for different centrality classes is shown for $p+$Al in Fig. 6, for $p+$Au in Fig. 7, and for ^{3}He +Au in Fig. 8.

Figures 9 and 10 show the nuclear modification factor as a function of p_T for 0%–100% $p+$Al, $p+$Au, and ^{3}He +Au collisions at backward and forward rapidity. The p_T dependence in different centrality classes is presented for $p+$Al in Fig. 11, for $p+$Au in Figs. 12 and 13, and for ^{3}He +Au in Fig. 14. The modification as a function of p_T in 0%–20% central collisions is compared between $p+$Al and $p+$Au in Fig. 15. Similar comparisons where the target is identical, but the projectile is different are shown for 0%–20% central collisions comparing $d+$Au and $p+$Au in Fig. 16 and comparing ^{3}He +Au and $p+$Au in Fig. 17.

The p_T integrated nuclear modification factor for $p+$Al, $p+$Au and ^{3}He +Au as a function of $\langle N_{\rm coll}\rangle$ is shown at both forward and backward rapidity in Figs. 18 and 19. A comparison between $p+$Al, $p+$Au and ^{3}He +Au modifications when plotted as a function of the average nuclear thickness sampled by the charmonium production is presented in Fig. 20. Figure 21 shows the mean p_T squared values for the three systems $p+$Al, $p+$Au, and ^{3}He +Au as a function of $\langle N_{\rm coll}\rangle$ for $p_T < 7$ GeV/c at forward and backward rapidity.

V. DISCUSSION

A. Rapidity dependence

The rapidity dependence of the modification for 0%–100% centrality, seen in Fig. 5, shows only weak modification for $p+$Al collisions. For both $p+$Au and ^{3}He +Au significant suppression is seen at forward rapidity, with less suppression at backward rapidity. The modifications for $p+$Au and ^{3}He +Au are very similar.

The rapidity dependence in three centrality bins for $p+$Al collisions, seen in Fig. 6, shows only weak modification in all centrality bins, both at forward and backward rapidity.

The $p+$Au data presented here contain finer centrality binning for central collisions than was previously available from $d+$Au. The rapidity dependence in six centrality bins for $p+$Au collisions, seen in Fig. 7, shows a factor of more than two suppression at the most forward rapidity in the 0%–5% centrality bin, and a marked increase in suppression with increasing rapidity in the forward direction. At backward rapidity, the modifications in all centrality bins show little centrality dependence, all being somewhat suppressed.

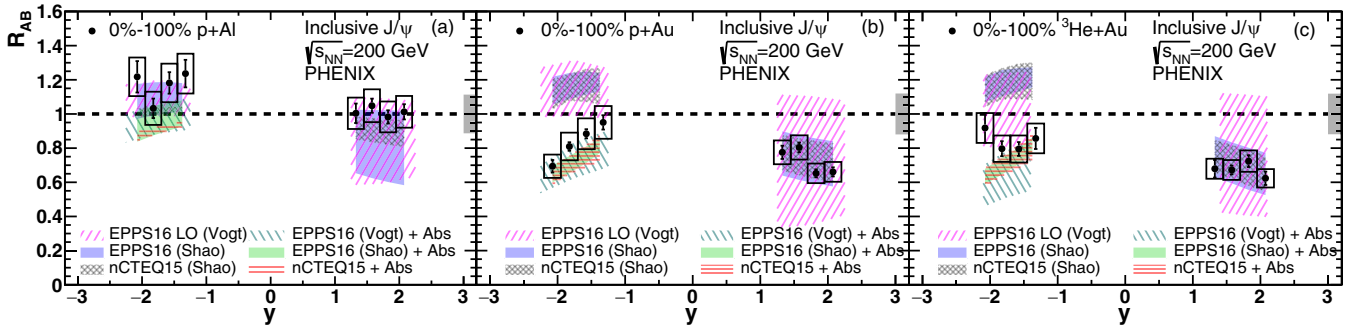

FIG. 5. Nuclear modification factor of inclusive J/ψ as a function of rapidity for 0%–100% $p+$Al (a), $p+$Au (b), and ^{3}He +Au (c) collisions. Bars (boxes) around data points represent point-to-point uncorrelated (correlated) uncertainties. The theory bands are discussed in the text.

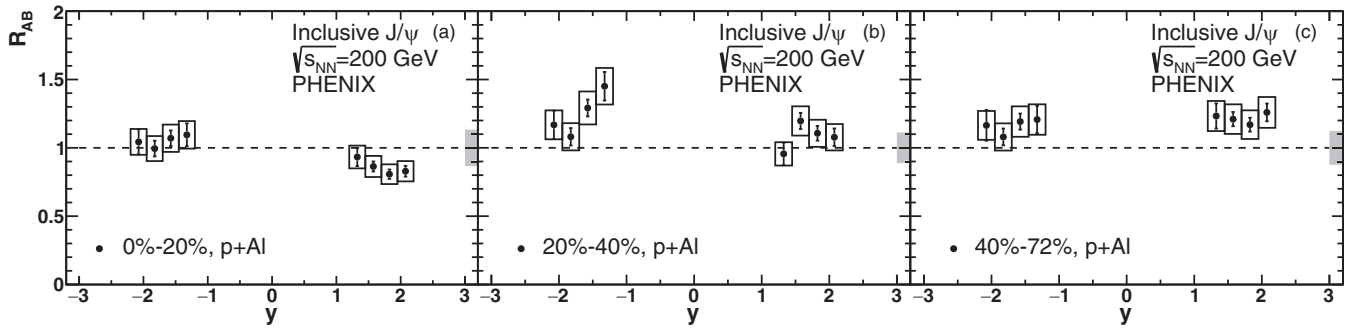

FIG. 6. Nuclear modification factor of inclusive J/ψ as a function of rapidity in three centrality bins for $p+$Al collisions. Bars (boxes) around data points represent point-to-point uncorrelated (correlated) uncertainties.

The rapidity dependence in three centrality bins for ^{3}He +Au collisions is shown in Fig 8. In comparison with the $p+$Al results shown in Fig. 6 for the 0%–20% centrality bin, which show little modification, the ^{3}He +Au results show a suppression at both forward and backward rapidity. The modification becomes less pronounced in the 20%–40% centrality range, and approaches unity for the most peripheral collisions within uncertainties.

The rapidity dependence of the 0%–100% centrality data is compared in Fig. 5 with model calculations from Vogt [50,51] and Shao *et al.* [52–55] showing the effect of nPDF modifications using the Eskola-Paakkinen-Paukkunen-Salgado (EPPS16) [1] next-to-leading order (NLO) and/or nuclear coordinated theoretical and experimental tests of quantum chromodynamics (nCTEQ15) NLO parameterizations [2]. The Vogt EPPS16 NLO shadowing calculations in general follow the methods described in [50], while the J/ψ mass and scale parameters are discussed in [51]. The Shao *et al.* model calculations for $p+$Au collisions are based on a Bayesian reweighting method which uses J/ψ constraints from $p+$Pb data at the LHC [52]. The dominant uncertainty in the reweighting method is the factorization scale dependence μ_F of the gluon modification factor $R_g^{Au}(x, \mu_F)$, where $\mu_F = \xi\mu_0$, with $\mu_0^2 = M^2 + {p_T}^2$ for the J/ψ transverse mass, and $\xi = 0.5$, 1, 2 for the factorization scale. The reweighting however is not applied for lighter ^{3}He and Al nuclei, with the predictions for these nuclei based on the original method described in [53–55]. For these predictions, the previous PHENIX J/ψ measurement in $p+p$ collisions [41] is used as a baseline. The calculations were performed at all three factorization scales (μ_0, 0.5 μ_0, and 2 μ_0) and provide two different confidence levels (68% and 90% CL). The uncertainty band shown is for the 68% CL, and we have taken the envelope of the uncertainty bands from the calculations at the three scales.

In Fig. 5, the calculations describe the data very well at forward rapidity for all three collision systems, and for $p+$Al at backward rapidity. For $p+$Au and ^{3}He +Au at backward rapidity the calculated modifications are too large by roughly 40%. However, the calculations do not contain effects of nuclear absorption, which is expected to be important at

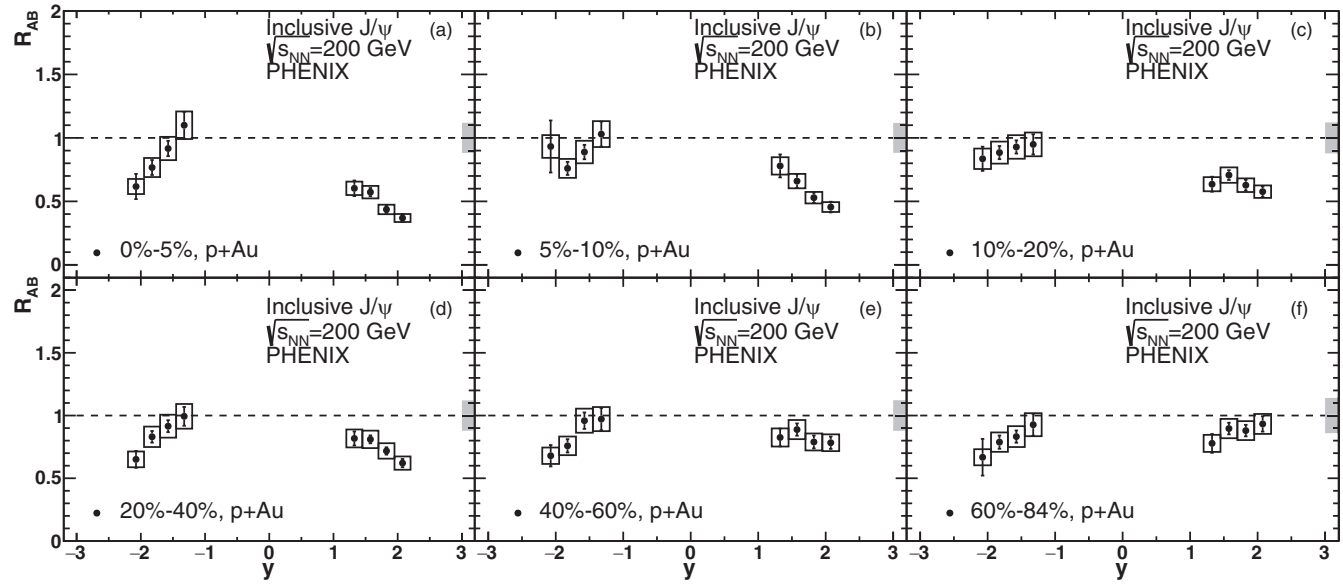

FIG. 7. Nuclear modification factor of inclusive J/ψ as a function of rapidity in six centrality bins for $p+$Au collisions. Bars (boxes) around data points represent point-to-point uncorrelated (correlated) uncertainties.

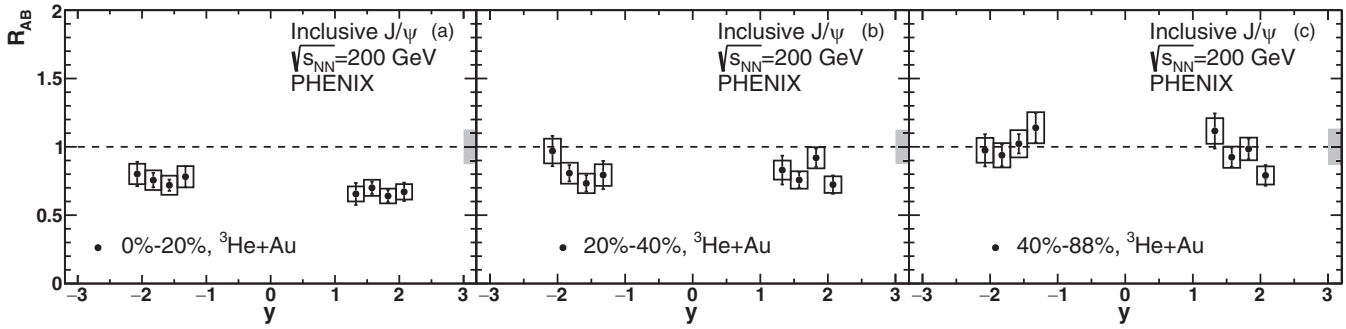

FIG. 8. Nuclear modification factor of inclusive J/ψ as a function of rapidity in three centrality bins for ^{3}He +Au collisions. Bars (boxes) around data points represent point-to-point uncorrelated (correlated) uncertainties.

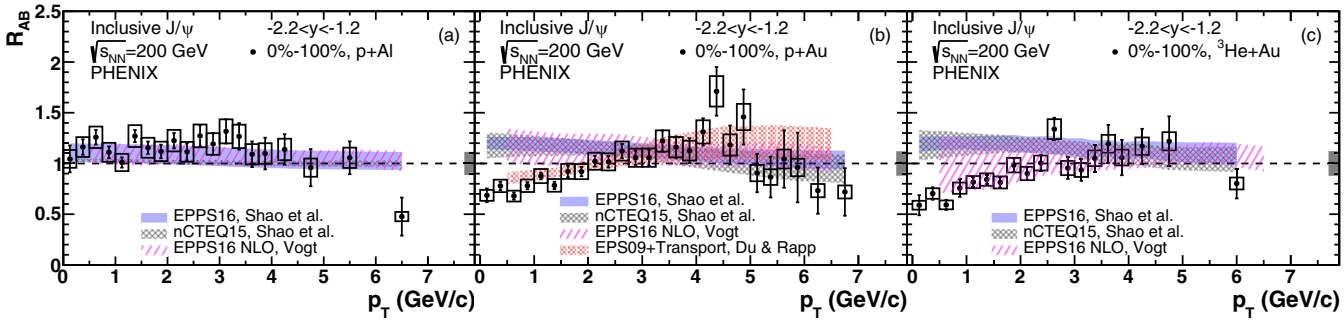

FIG. 9. Nuclear modification factor of inclusive J/ψ as a function of p_T at backward rapidity (Al/Au-going direction) for 0%–100% $p+$Al, $p+$Au, and ^{3}He +Au collisions. Bars (boxes) around data points represent point-to-point uncorrelated (correlated) uncertainties. The theory bands are discussed in the text.

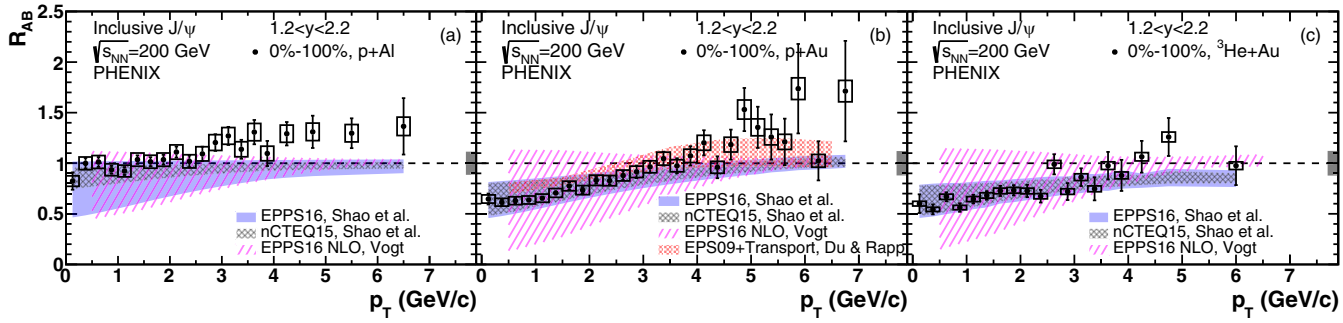

FIG. 10. Nuclear modification factor of inclusive J/ψ as a function of p_T at forward rapidity ($p/^3$He-going direction) for 0%–100% $p+$Al, $p+$Au, and ^{3}He +Au collisions. Bars (boxes) around data points represent point-to-point uncorrelated (correlated) uncertainties. The theory bands are discussed in the text.

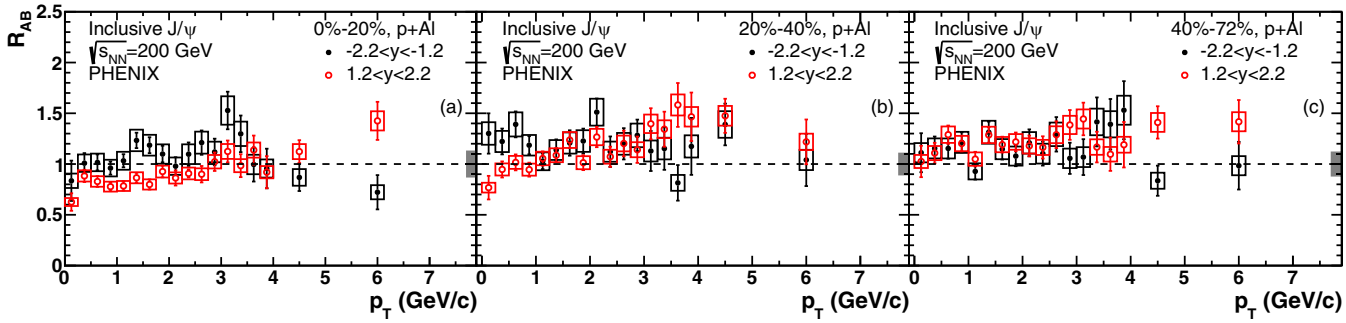

FIG. 11. Nuclear modification factor of inclusive J/ψ as a function of p_T in three centrality bins for $p+$Al collisions. Bars (boxes) around data points represent point-to-point uncorrelated (correlated) uncertainties.

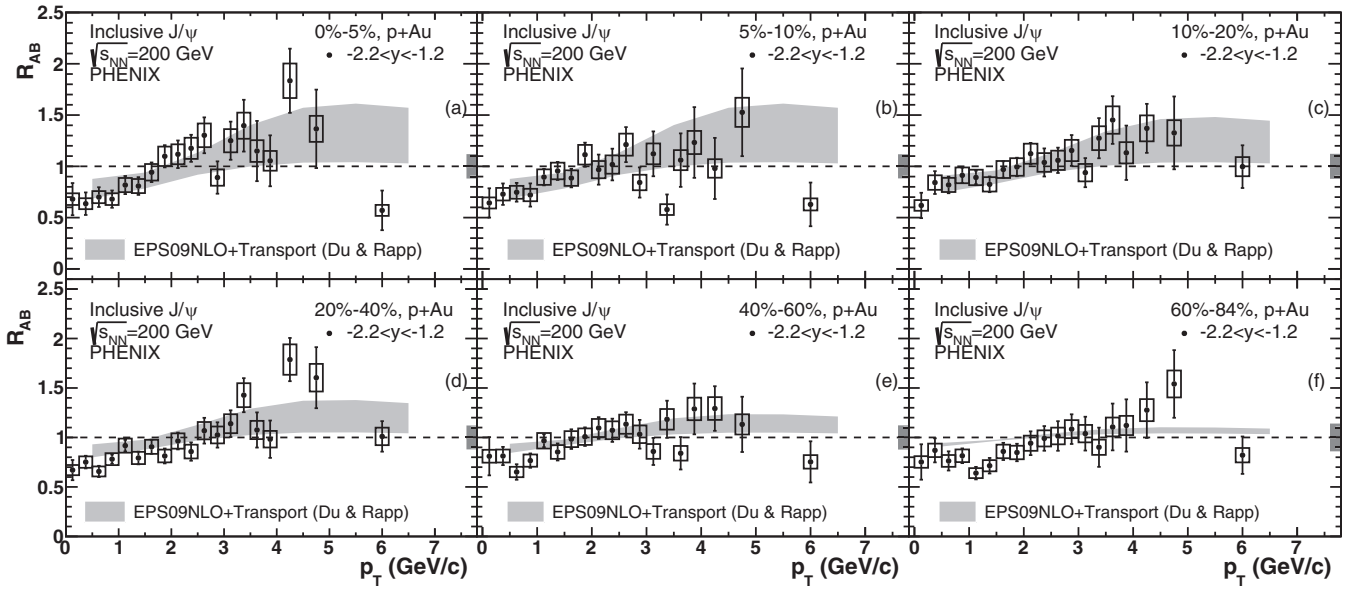

FIG. 12. Nuclear modification factor of inclusive J/ψ as a function of p_T at $-2.2 < y < -1.2$ in six centrality bins for $p+$Au collisions. Bars (boxes) around data points represents point-to-point uncorrelated (correlated) uncertainties. The theory bands are discussed in the text. Note that the theory bands compared with the 0%–5% and 5%–10% centrality data are for 0%–10%.

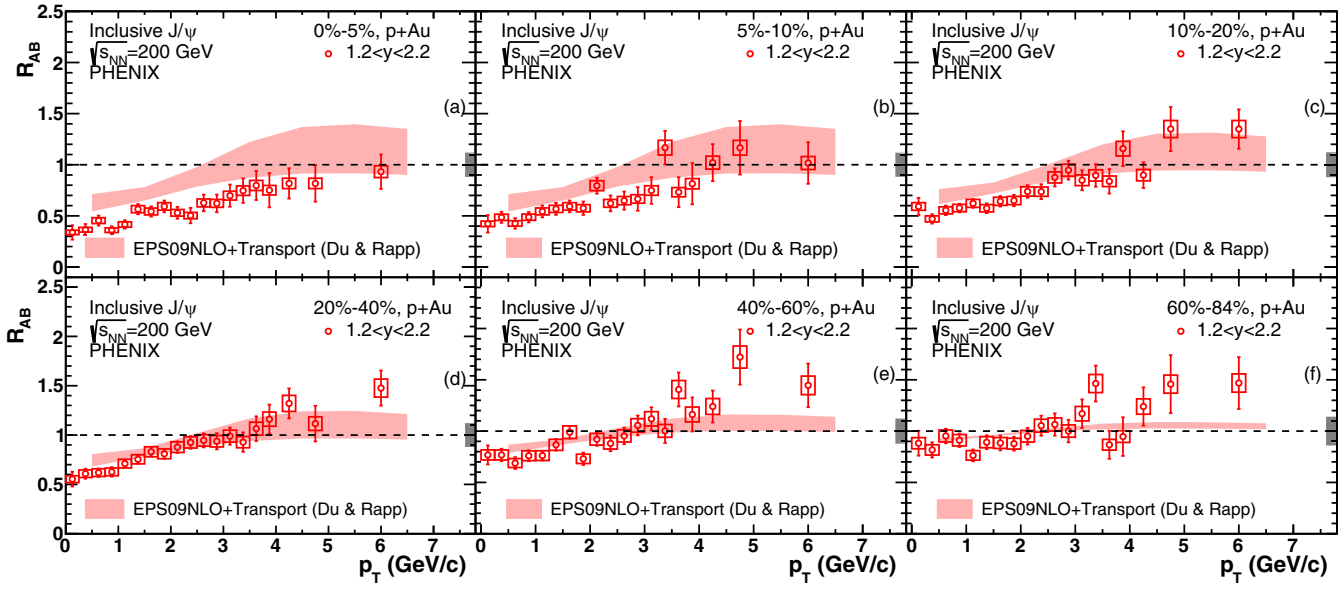

FIG. 13. Nuclear modification factor of inclusive J/ψ as a function of p_T at $1.2 < y < 2.2$ in six centrality bins for $p+$Au collisions. The theory bands are discussed in the text. Note that the theory bands compared with the 0%–5% and 5%–10% centrality data are for 0%–10%.

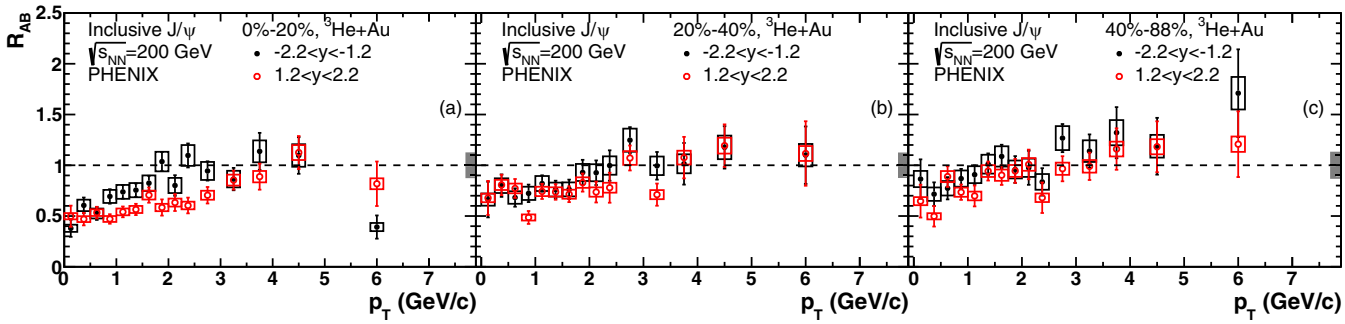

FIG. 14. Nuclear modification factor of inclusive J/ψ as a function of p_T in three centrality bins for ^{3}He +Au collisions.

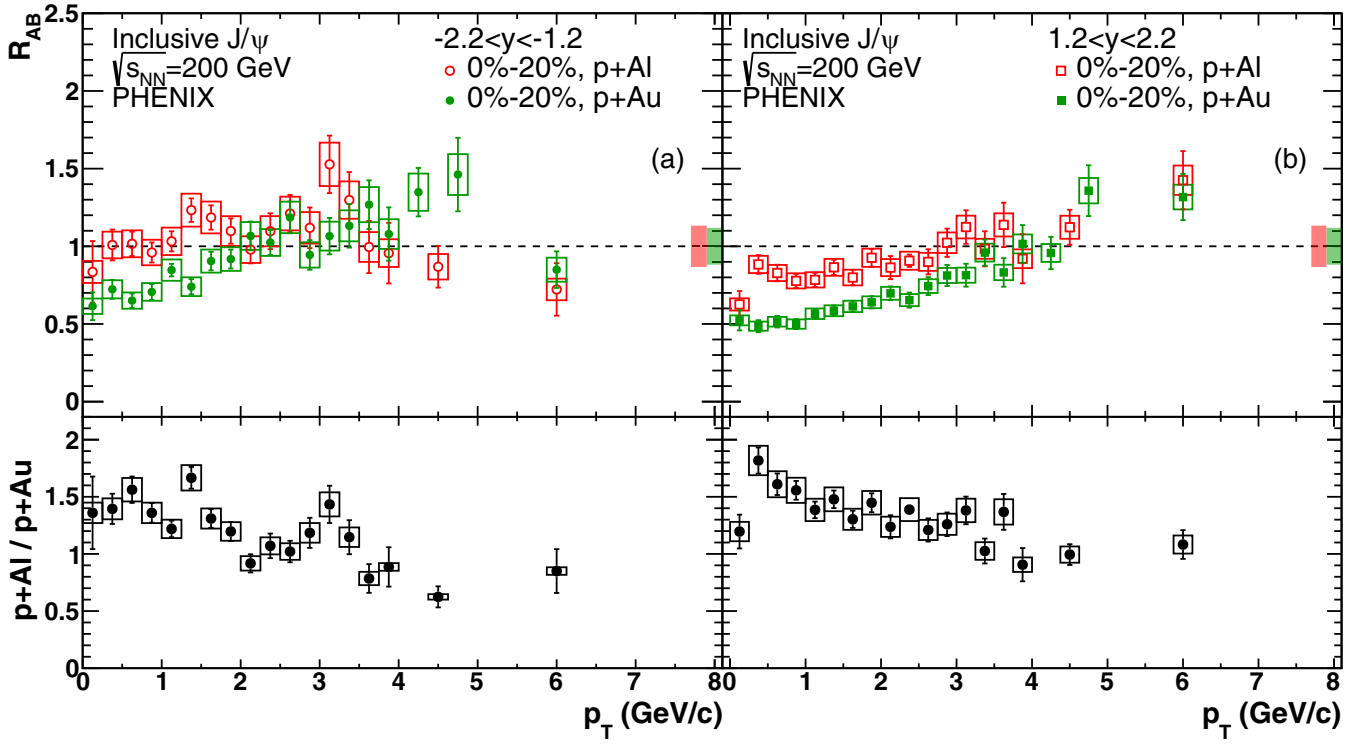

FIG. 15. Comparison of nuclear modification factor of J/ψ as a function of p_T in 0%–20% centrality $p+$Al and $p+$Au collisions. Bars (boxes) around data points represent point-to-point uncorrelated (correlated) uncertainties.

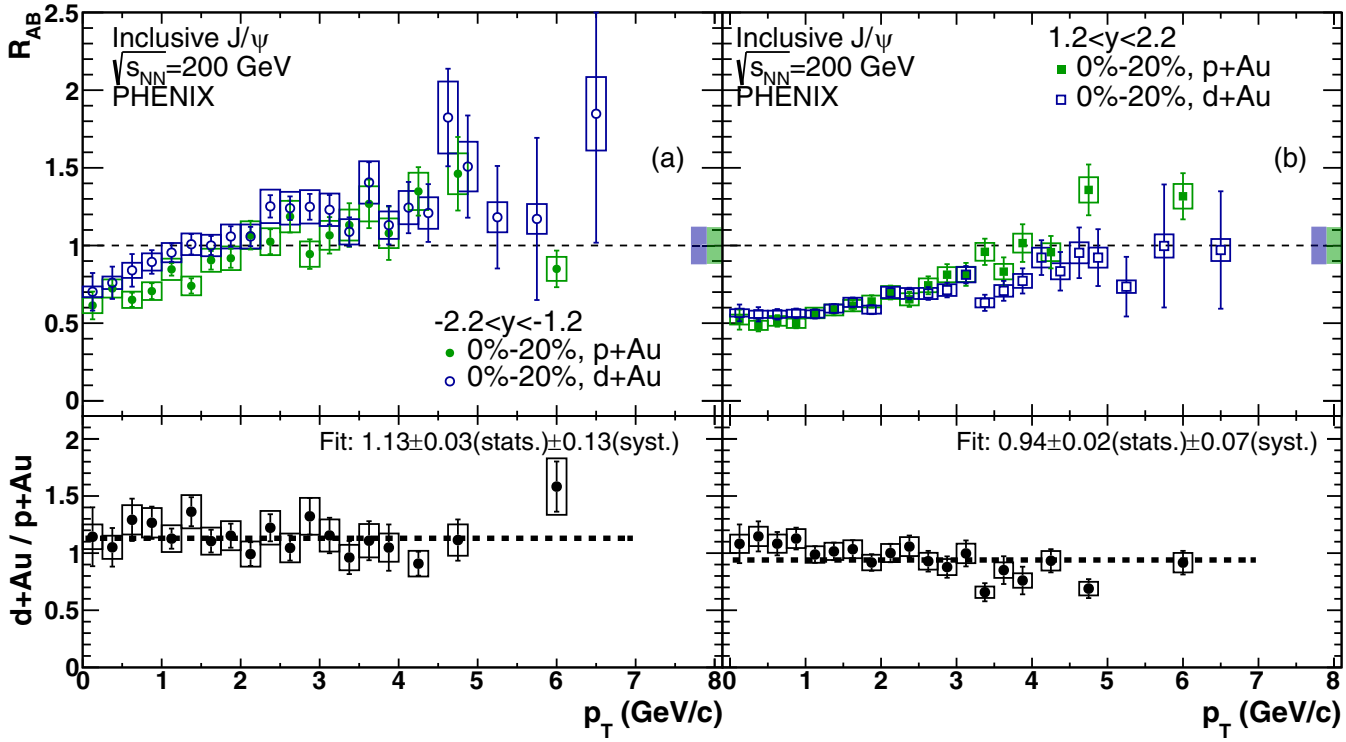

FIG. 16. Comparison of nuclear modification factor of J/ψ as a function of p_T in 0%–20% centrality $d+$Au [10] and $p+$Au collisions. Bars (boxes) around data points represent point-to-point uncorrelated (correlated) uncertainties.

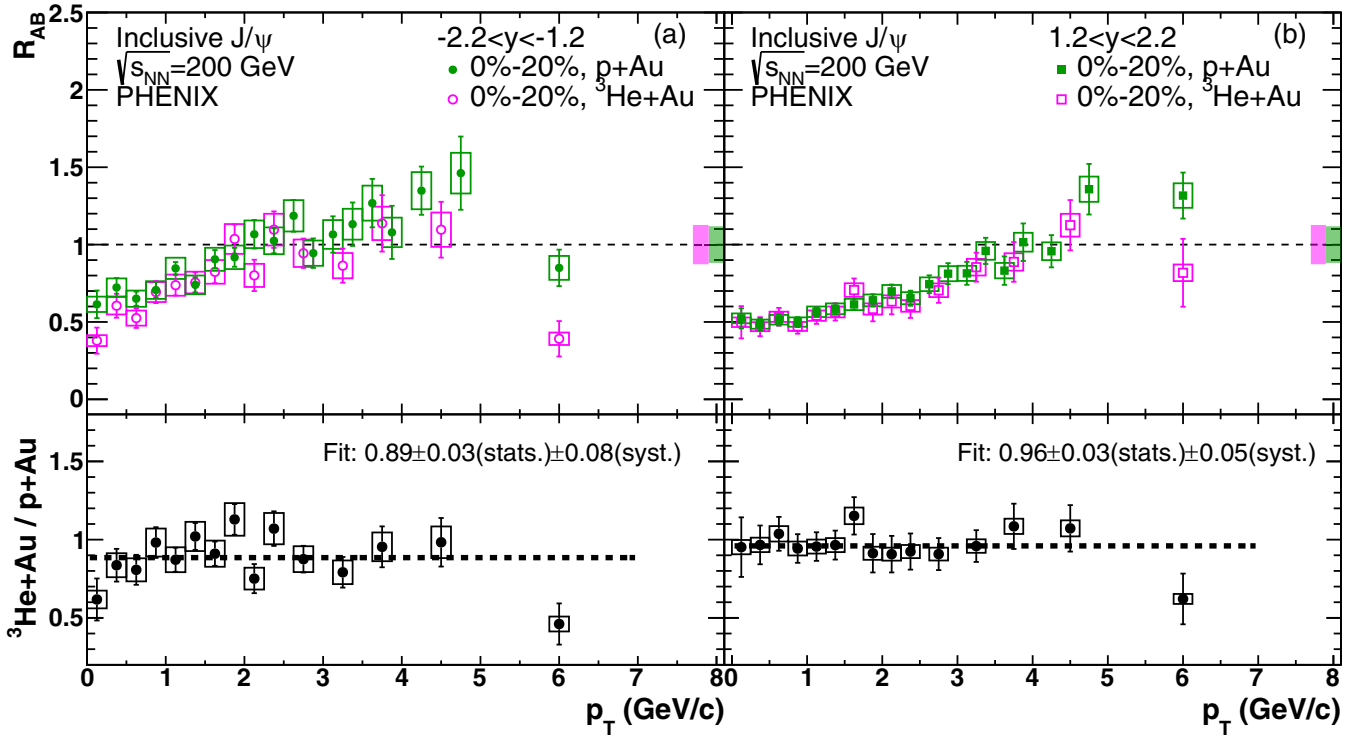

FIG. 17. Comparison of nuclear modification factor of J/ψ as a function of p_T in 0%–20% centrality $p+$ Au and ^{3}He +Au collisions. Bars (boxes) around data points represent point-to-point uncorrelated (correlated) uncertainties.

backward rapidity at $\sqrt{s_{NN}} = 200$ GeV [4], where the nuclear crossing time is comparable with the charmonium formation time. That is not expected to be the case at forward rapidity at $\sqrt{s_{NN}} = 200$ GeV, or at the rapidities of interest at LHC energies. Because nuclear absorption is not included in the model calculations, they should be expected to overpredict the modification in $p+$ Au and ^{3}He +Au at backward rapidity.

An estimate of the effect of nuclear absorption at backward rapidity can be obtained from a model [5] fitted to absorption cross sections derived from shadowing corrected data measured at a broad range of beam energies [4]. The model assumes that the $c\bar{c}$ pair size grows linearly with time until it reaches the size of a fully formed charmonium meson. Then the absorption cross section depends on the proper time before the pair escapes the target. The effect of the modification due to nuclear absorption at backward rapidity from this model is added to Fig. 5, by folding it into the shadowing calculation. The results indicate that the measured modifications are reasonably consistent with shadowing plus nuclear absorption.

B. p_T dependence

The p_T dependence for 0%–100% centrality, seen at backward rapidity in Fig. 9 and at forward rapidity in Fig. 10,

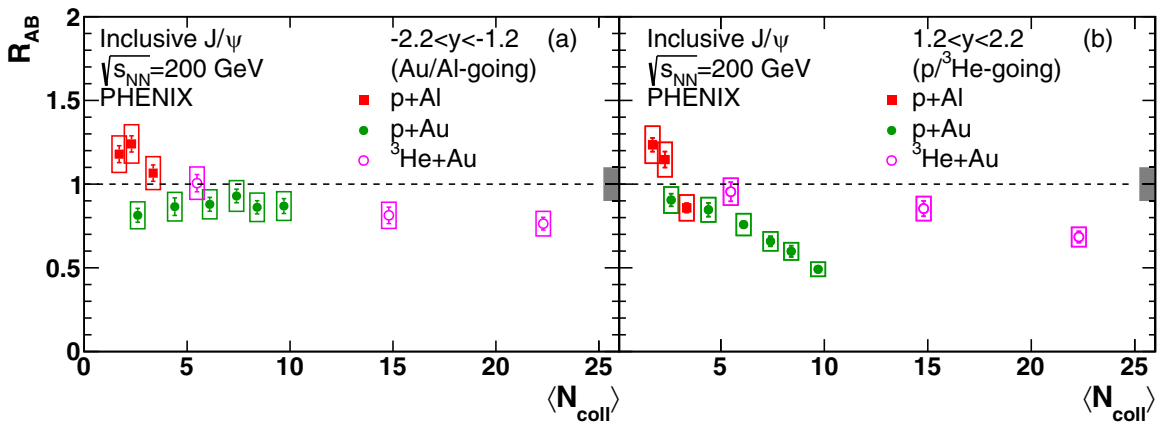

FIG. 18. Nuclear modification factor of J/ψ as a function of $\langle N_{\rm coll}\rangle$ for $p+$ Al, $p+$ Au, and ^{3}He +Au collisions. Bars (boxes) around data points represent point-to-point uncorrelated (correlated) uncertainties.

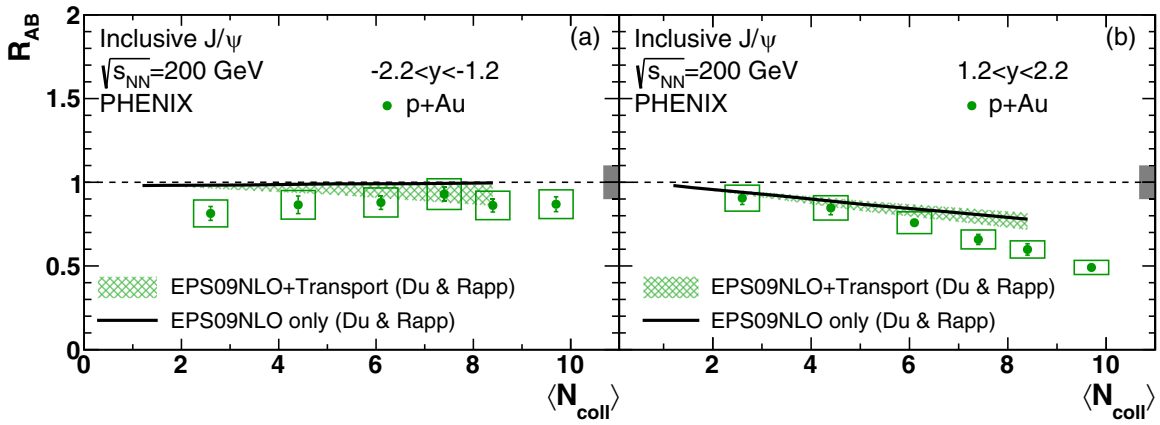

FIG. 19. Nuclear modification factor of J/ψ as a function of $\langle N_{\rm coll}\rangle$ for $p+$ Au collisions compared with the transport model. Bars (boxes) around data points represent point-to-point uncorrelated (correlated) uncertainties.

shows little modification for $p+$ Al but shows strong, and similar, p_T dependence for $p+$ Au and ^{3}He +Au. These data are also compared with the calculations of Shao *et al.* [52]. As for the rapidity dependence, the calculations describe the forward rapidity data well for all three collision systems and for the backward rapidity $p+$ Al. But the backward rapidity modification for $p+$ Au and ^{3}He +Au is overpredicted. Significant nuclear absorption is expected at backward rapidity and low p_T, and calculations that do not include it should overpredict the modification there.

The $p+$ Au modifications vs p_T, seen at forward rapidity in Fig. 13 for all centrality bins, shows very strong dependence on centrality. The modification falls to 0.35 at low p_T for the 5% most central collisions. At backward rapidity, as shown in Fig. 12, the suppression is considerably weaker at low p_T for the most central collisions, but it changes more slowly with centrality. The result is that for collision centralities above 20% the behavior of the modification versus p_T becomes rather similar at forward and backward rapidity. The p_T dependence of the nuclear modification factors in $p+$ Al and ^{3}He +Au collisions are shown in Figs. 11 and 14, respectively.

We see little modification across all three centrality ranges of $p+$ Al collisions, as was the case for the rapidity dependent results shown in Fig. 6. The $p+$ Al nuclear modification factor for the 6–7 GeV/c data point seen in Fig. 9(a) is quite low. However, the 6 GeV/c (5–7 GeV/c bin) points for the three backward rapidity centrality bins shown in Fig. 11 do not exhibit the same behavior. We have therefore interpreted this last data point as being a deviation from the trend. In 0%–20% ^{3}He +Au collisions, a suppression is observed at both forward and backward rapidity, and the modification becomes weaker in higher p_T. The modification is strongest in most central collisions, and the R_{AB} approaches unity for the most peripheral collisions. As seen with $p+$ Al, the last data point (5–7 GeV/c bin) for ^{3}He +Au is also quite low. Likewise, we have interpreted this behavior as being a deviation from the trend, considering the measurements shown in Fig. 9(c) do not produce a similar effect.

The theory predictions shown in Figs. 12 and 13 are the results of adapted transport models provided by Du and Rapp, based on the original transport model by Zhao and Rapp for $A+A$ collisions [56]. The theory was extended for

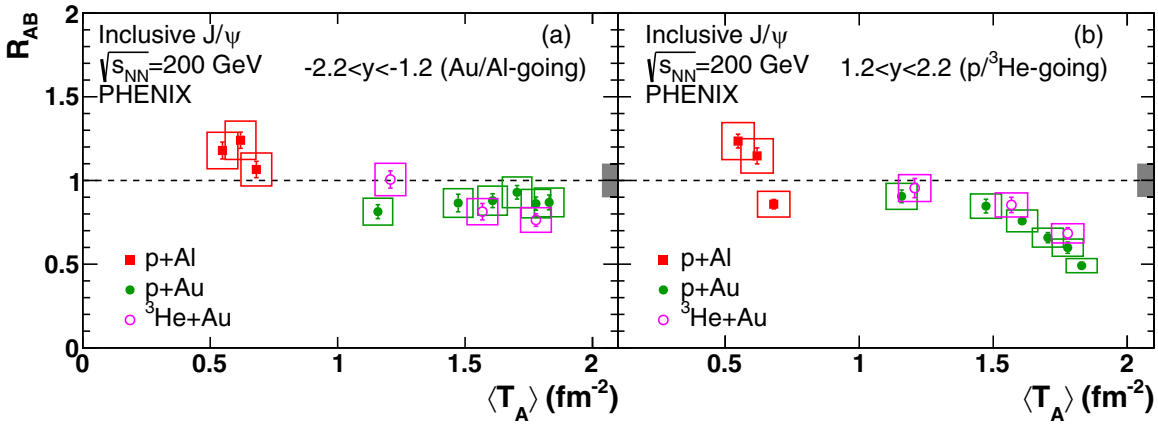

FIG. 20. Nuclear modification factor of J/ψ as a function of the mean target thickness sampled by charmonium production in the centrality bin, for $p+$ Al, $p+$ Au and ^{3}He +Au collisions. Bars (boxes) around data points represent point-to-point uncorrelated (correlated) uncertainties.

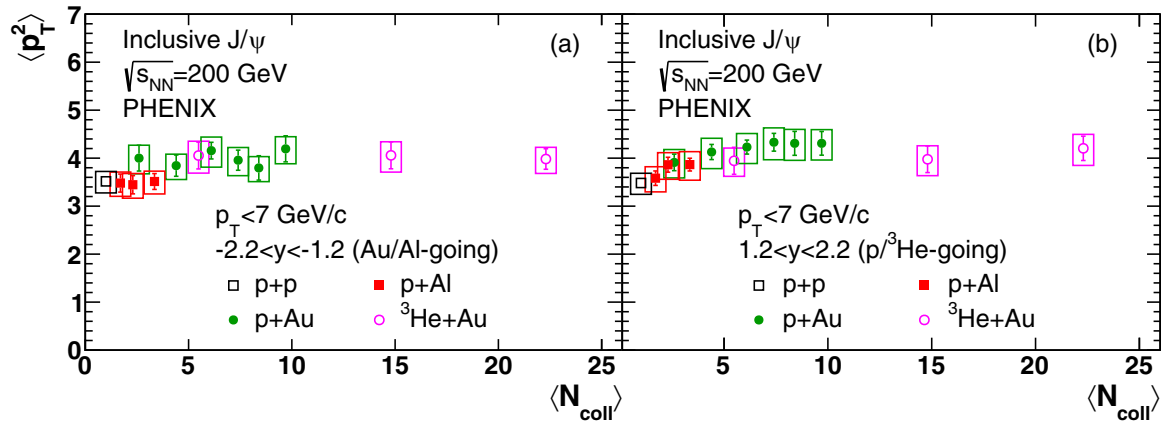

FIG. 21. $\langle p_T^2 \rangle$ of J/ψ for $p_T < 7\,\mathrm{GeV}/c$ as a function of $\langle N_{\mathrm{coll}} \rangle$ for $p+\mathrm{Al}$, $p+\mathrm{Au}$, and $^3\mathrm{He}+\mathrm{Au}$ collisions. Bars (boxes) around data points represent point-to-point uncorrelated (correlated) uncertainties.

$d+A$ collisions [28] and most recently for $p+A$ collisions [57]. The transport model includes a fireball generated by a Monte Carlo Glauber model [58] in addition to shadowing from Eskola-Paukkunen-Salgado (EPS09) [59] NLO, a broadening parameter [60], and an absorption cross section constrained by PHENIX $d+\mathrm{Au}$ data [11]. The J/ψ production cross section is described in [57], and charged particle multiplicity [61], hadronic dissociation rates [28], and open charm production cross sections [57] are also considered. The calculations reproduce the data at high p_T, but generally underpredict the suppression at low p_T at forward rapidity. Because the modification of J/ψ production in the transport model is not very strong at forward rapidity, the suppression there is dominated by the EPS09 shadowing contribution.

In a previous PHENIX measurement of charged particle multiplicity [61], it was found that twice as many particles are produced in 0%–20% central $p+\mathrm{Au}$ collisions than in 0%–20% central $p+\mathrm{Al}$ collisions, and the multiplicity in 0%–20% $^3\mathrm{He}+\mathrm{Au}$ collisions is about a factor of two larger than in 0%–20% $p+\mathrm{Au}$ collisions. To look for evidence of an effect from this, Figs. 15, 16, and 17 show direct comparisons between the modifications in the 0%–20% centrality bin of different projectile ($p/d/^3\mathrm{He}$) and target sizes (Al/Au). The ratio of nuclear modification factors is included in the bottom panel. In the comparisons among $p+\mathrm{Al}$, $p+\mathrm{Au}$, and $^3\mathrm{He}+\mathrm{Au}$ collisions, all systematic uncertainties from each collision system are included except the initial shape uncertainty, which cancels upon taking the ratio, and all systematic uncertainties stemming from the $p+p$ system cancel. In the comparison between $p+\mathrm{Au}$ and $d+\mathrm{Au}$, the two systems do not share the same $p+p$ reference, therefore all systematic uncertainties are included in the ratio. Note the $d+\mathrm{Au}$ data set was recorded in 2008, while the $p+\mathrm{Au}$ data was recorded in 2015 with a new detector. Simulations for $d+\mathrm{Au}$ were also performed using methods that differ from those used for the new small systems study. For $p+\mathrm{Au}$, $d+\mathrm{Au}$ and $^3\mathrm{He}+\mathrm{Au}$ comparisons, a mean value has been fitted to the ratios, and the result is shown on the plot together with the fit uncertainty and the uncertainty from the systematic errors. The systematic uncertainty was determined by repeating the fit with all points moved to the upper or lower limits of their systematic uncertainty.

The comparison in Fig. 15 of 0%–20% $p+\mathrm{Al}$ with 0%–20% $p+\mathrm{Au}$ modifications contrasts the weak modification in central $p+\mathrm{Al}$ collisions with the strong modification, particularly at forward rapidity, in central $p+\mathrm{Au}$ collisions. Figure 15(a) shows $p+\mathrm{Au}$ with a nuclear modification factor of about 0.85 at 6 GeV/c (5–7 GeV/c bin). A drop in modification at high p_T is expected due to shadowing (and possibly also k_T broadening). The comparison in Fig. 16 of 0%–20% $p+\mathrm{Au}$ with 0%–20% $d+\mathrm{Au}$ modifications highlights the similarity between the two systems. A fit to the ratio of $d+\mathrm{Au}$ to $p+\mathrm{Au}$ at forward rapidity was found to be $1.13 \pm 0.03(\mathrm{stat}) \pm 0.13(\mathrm{syst})$ and at backward rapidity is $0.94 \pm 0.02(\mathrm{stat}) \pm 0.07(\mathrm{syst})$.

In the comparison between 0%–20% $p+\mathrm{Au}$ and 0%–20% $^3\mathrm{He}+\mathrm{Au}$ collisions shown in Fig. 17, the ratio at forward rapidity is

$$\overline{R_{^3\mathrm{HeAu}}/R_{\mathrm{pAu}}} = 0.96 \pm 0.03(\mathrm{stat}) \pm 0.05(\mathrm{syst}),$$

which is consistent with unity. At backward rapidity the ratio is

$$\overline{R_{^3\mathrm{HeAu}}/R_{\mathrm{pAu}}} = 0.89 \pm 0.03(\mathrm{stat}) \pm 0.08(\mathrm{syst}).$$

There may be deviations from the trend in the highest p_T bin, but large statistical uncertainties preclude firm conclusions. The results are consistent with J/ψ production being reduced for the $^3\mathrm{He}$ projectile, with the backward rapidity ratio having a probability of 90% of being less than one.

C. $\langle N_{\mathrm{coll}} \rangle$ dependence

The p_T integrated modifications as a function of $\langle N_{\mathrm{coll}} \rangle$ in each centrality bin are shown in Fig. 18 for the three systems $p+\mathrm{Al}$, $p+\mathrm{Au}$ and $^3\mathrm{He}+\mathrm{Au}$. No scaling with $\langle N_{\mathrm{coll}} \rangle$ is expected between $p+\mathrm{Au}$ and $^3\mathrm{He}+\mathrm{Au}$, because $^3\mathrm{He}+\mathrm{Au}$ will have roughly three times as many collisions as $p+\mathrm{Au}$ in the same centrality class. The $\langle N_{\mathrm{coll}} \rangle$ dependence of the $p+\mathrm{Au}$ modification is shown again in Fig. 19, where it is compared with the p_T integrated modification predicted by Du and Rapp. The theory calculation shows both the

CNM baseline and the result of the transport calculations. At backward rapidity some nuclear absorption is expected. At forward rapidity, it appears that the CNM effects are not strong enough to explain the data. However, the model predicts a suppression beyond CNM effects at backward rapidity for central collisions of approximately 10%.

Modifications that are due to CNM effects (including nuclear absorption) would be expected to depend on the thickness of the target nucleus at the impact parameter of the nucleon that was involved in the hard process. The nuclear thickness can be written

$$T_A(r_T) = \int \rho_A(z, r_T)\, dz, \tag{8}$$

where $\rho_A(z, r_T)$ is the density distribution of nucleons in nucleus A taken from the Woods-Saxon distribution used in the Glauber model discussed in Sec. II. The parameter z is the location in the nucleus along the beam direction, and r_T is the transverse distance from the center of the nucleus. $T_A(r_T)$ is the average number of nucleons per unit area at the projectile nucleon impact parameter r_T. To get the average value of T_A sampled for charmonium production within a given centrality bin, the values of $T_A(r_T)$ are weighted by the distribution of r_T values within the centrality bin, to reflect the number of projectile nucleons having one or more inelastic collisions at that r_T, and additionally by the probability of a hard process at that r_T—which is proportional to $T_A(r_T)$.

Figure 20 shows the $p+$Al, $p+$Au and ^{3}He +Au modifications plotted versus $\langle T_A \rangle$, in each centrality bin. The modifications seem to fall on a common curve within uncertainties, as would be expected if they were primarily due to CNM effects.

The $\langle p_T^2 \rangle$ values versus $\langle N_{\rm coll} \rangle$, shown in Fig. 21, fall on a common curve for all three systems. The $\langle N_{\rm coll} \rangle$ dependence is mild, with $\langle p_T^2 \rangle$ increasing from 3.3 in $p+p$ collisions to approximately 4.0 in $p+$Au and ^{3}He +Au collisions. The $\langle p_T^2 \rangle$ is very similar between forward and backward rapidity, as was also observed in $d+$Au collisions [10].

VI. SUMMARY AND CONCLUSIONS

We have presented invariant yields for inclusive J/ψ production in $p+p$, $p+$Al, $p+$Au and ^{3}He +Au collisions at $\sqrt{s_{NN}} = 200$ GeV, and the corresponding nuclear modifications for $p+$Al, $p+$Au and ^{3}He +Au. The new $p+$Au results are found to agree within uncertainties with the previous PHENIX $d+$Au results [9].

The $p+$Al modifications are found to be much weaker at all centralities than those in $p+$Au. The 0%–100% centrality data for $p+$Al are found to be well described in rapidity and p_T by calculations containing only shadowing effects from the EPPS16 NLO and nCTEQ15 NLO parametrizations, aside from slightly underpredicting the modification at 4–6 GeV/c at forward rapidity.

The 0%–100% centrality $p+$Au and ^{3}He +Au data are also compared with calculations based on the EPPS16 NLO and nCTEQ15 NLO shadowing parametrizations. At forward rapidity, the calculations describe the $p+$Au and ^{3}He +Au modifications well in both rapidity and p_T, again with the exception of slightly underpredicting the modification at 4–6 GeV/c at forward rapidity. At backward rapidity, the calculations overpredict the modifications. We found that adding the predicted nuclear absorption modification taken from previous work to the backward rapidity p_T integrated data reduced the modifications to values consistent with the data.

The ratio of the ^{3}He +Au and $p+$Au modifications for the 0%–20% centrality bin at forward rapidity is

$$\overline{R_{^3\mathrm{HeAu}}/R_{\mathrm{pAu}}} = 0.96 \pm 0.03(\mathrm{stat}) \pm 0.05(\mathrm{syst}),$$

which is smaller but consistent with unity. At backward rapidity it is

$$\overline{R_{^3\mathrm{HeAu}}/R_{\mathrm{pAu}}} = 0.89 \pm 0.03(\mathrm{stat}) \pm 0.08(\mathrm{syst}).$$

The results are consistent with a reduction in the modification for the heavier projectile case. Given the systematic uncertainty, the backward rapidity ratio has a 90% probability of being less than 1.0.

For $p+$Au at forward rapidity, the nuclear modification vs p_T shows very strong centrality dependence, dropping to approximately 0.35 at low p_T in the most central 5% of collisions. At backward rapidity the suppression is weaker for central collisions, but it changes more slowly. Comparison with theory calculations that include EPS09 shadowing and a final state transport model are able to reproduce the general shape of the p_T dependence at each centrality, but greatly underpredict the suppression at low p_T for central collisions.

The p_T integrated modification for $p+$Au drops steeply with centrality at forward rapidity, reaching approximately 0.5 for the 5% most central collisions. The modification at backward rapidity is found to have weak centrality dependence. Because nuclear absorption is evidently important at backward rapidity, the weak centrality dependence there is likely due to a trade-off between antishadowing and nuclear absorption. It was found that plotting the modification vs $\langle T_A \rangle$ for each centrality bin caused them to fall on a common line for all three systems, as would be expected if CNM effects dominate.

ACKNOWLEDGMENTS

We thank the staff of the Collider-Accelerator and Physics Departments at Brookhaven National Laboratory and the staff of the other PHENIX participating institutions for their vital contributions. We also thank H.-S. Shao and J.-P. Lansberg *et al.*, R. Vogt, X. Du, and R. Rapp for useful discussions and providing unpublished predictions. We acknowledge support from the Office of Nuclear Physics in the Office of Science of the Department of Energy, the National Science Foundation, Abilene Christian University Research Council, Research Foundation of SUNY, and Dean of the College of Arts and Sciences, Vanderbilt University (U.S.A), Ministry of Education, Culture, Sports, Science, and Technology and the Japan Society for the Promotion of Science (Japan), Conselho Nacional de Desenvolvimento Científico e Tecnológico and

Fundação de Amparo à Pesquisa do Estado de São Paulo (Brazil), Natural Science Foundation of China (People's Republic of China), Croatian Science Foundation and Ministry of Science and Education (Croatia), Ministry of Education, Youth and Sports (Czech Republic), Centre National de la Recherche Scientifique, Commissariat à l'Énergie Atomique, and Institut National de Physique Nucléaire et de Physique des Particules (France), Bundesministerium für Bildung und Forschung, Deutscher Akademischer Austausch Dienst, and Alexander von Humboldt Stiftung (Germany), J. Bolyai Research Scholarship, EFOP, the New National Excellence Program (ÚNKP), NKFIH, and OTKA (Hungary), Department of Atomic Energy and Department of Science and Technology (India), Israel Science Foundation (Israel), Basic Science Research and SRC(CENuM) Programs through NRF funded by the Ministry of Education and the Ministry of Science and ICT (Korea). Physics Department, Lahore University of Management Sciences (Pakistan), Ministry of Education and Science, Russian Academy of Sciences, Federal Agency of Atomic Energy (Russia), VR and Wallenberg Foundation (Sweden), the U.S. Civilian Research and Development Foundation for the Independent States of the Former Soviet Union, the Hungarian American Enterprise Scholarship Fund, the US-Hungarian Fulbright Foundation, and the US-Israel Binational Science Foundation.

APPENDIX

The invariant yields for all data sets are presented in this Appendix. Figure 22 shows inclusive J/ψ invariant yield as a function of rapidity in MB $p+p$, $p+$Al, $p+$Au, and ^{3}He $+$Au collisions, and the invariant yields in $p+$Al, $p+$Au, and ^{3}He $+$Au collisions are scaled with $\langle N_{\rm coll}\rangle$ to compare with the invariant yield in $p+p$ collisions. In this and the following figures showing results of invariant yield measurement, the bars (boxes) around data points represent point-to-point uncorrelated (correlated) uncertainties. Figures. 23, 24, and 25 show inclusive J/ψ invariant yield as a function of rapidity in different centrality of $p+$Al, $p+$Au, and ^{3}He $+$Au collisions, respectively. Invariant yields in $p+$Al, $p+$Au, and ^{3}He $+$Au collisions are scaled with $\langle N_{\rm coll}\rangle$, and the $p+p$ result is also presented in each panel. Figures 26, 27, and 28 show inclusive J/ψ invariant yield as a function of p_T in different centrality of $p+$Al, $p+$Au, and ^{3}He $+$Au collisions, respectively.

At $p_T > 2.5\,{\rm GeV}/c$, p_T binning was changed for different data sets depending on statistics as described in Table IV. When calculating the nuclear modification factor for p_T bins of different Δp_T from the $p+p$ data, additional fits to the $p+p$ data were performed to match the p_T binning of the $p/^3$He $+A$ data.

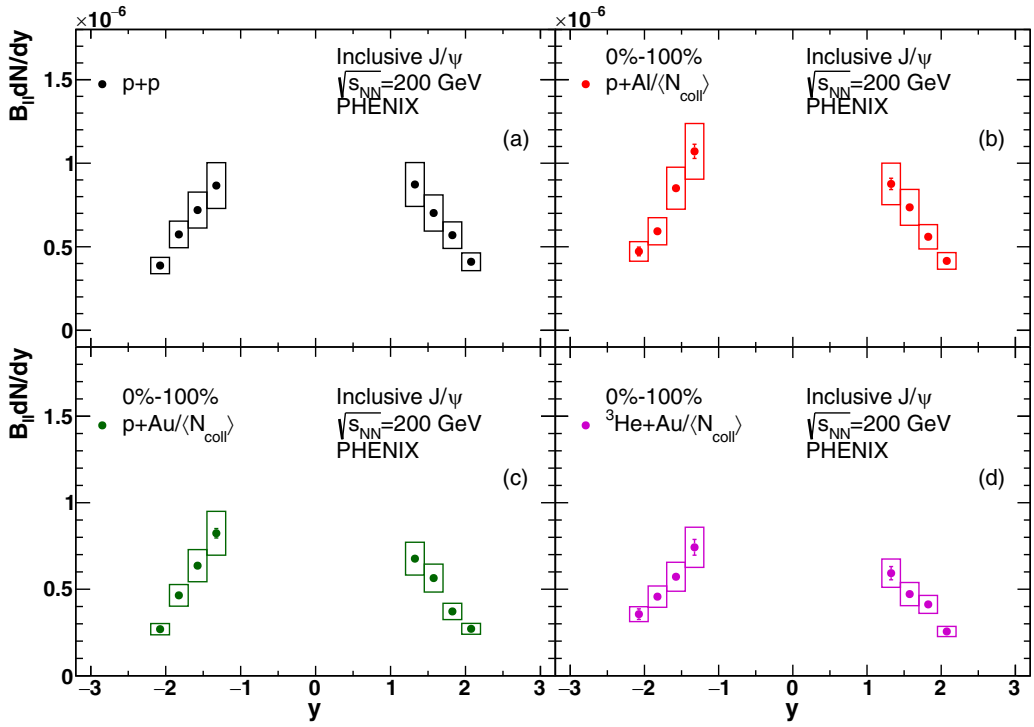

FIG. 22. J/ψ invariant yield as a function of y in MB $p+p$, $p+$Al, $p+$Au, and ^{3}He $+$Au collisions. Bars (boxes) around data points represents point-to-point uncorrelated (correlated) uncertainties. There is also a global uncertainty of 10.1%, 11.5%, 12.1%, and 12.2% corresponding to $p+p$, $p+$Al, $p+$Au and ^{3}He $+$Au yields.

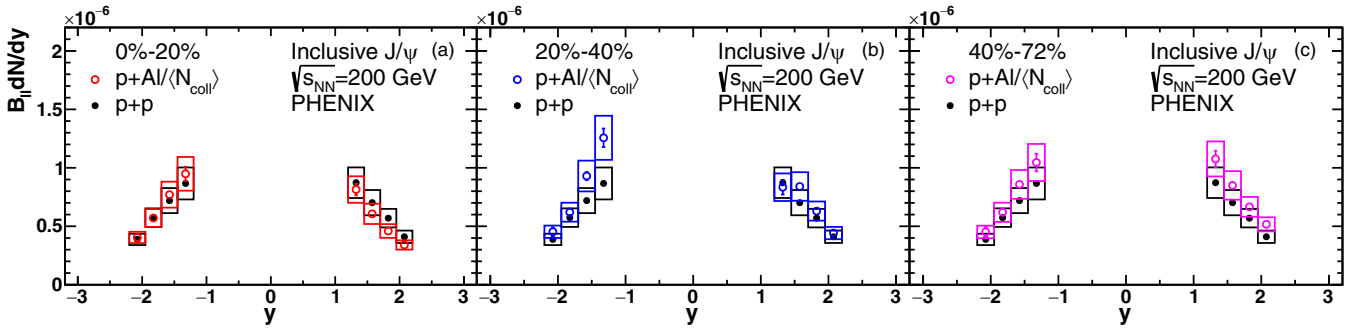

FIG. 23. J/ψ invariant yield as a function of y in various centrality bins of $p+$Al collisions. Bars (boxes) around data points represents point-to-point uncorrelated (correlated) uncertainties. There is also a global uncertainty of 13.6%, 12.2%, and 12.3% corresponding to 0%–20%, 20%–40%, and 40%–72% centrality.

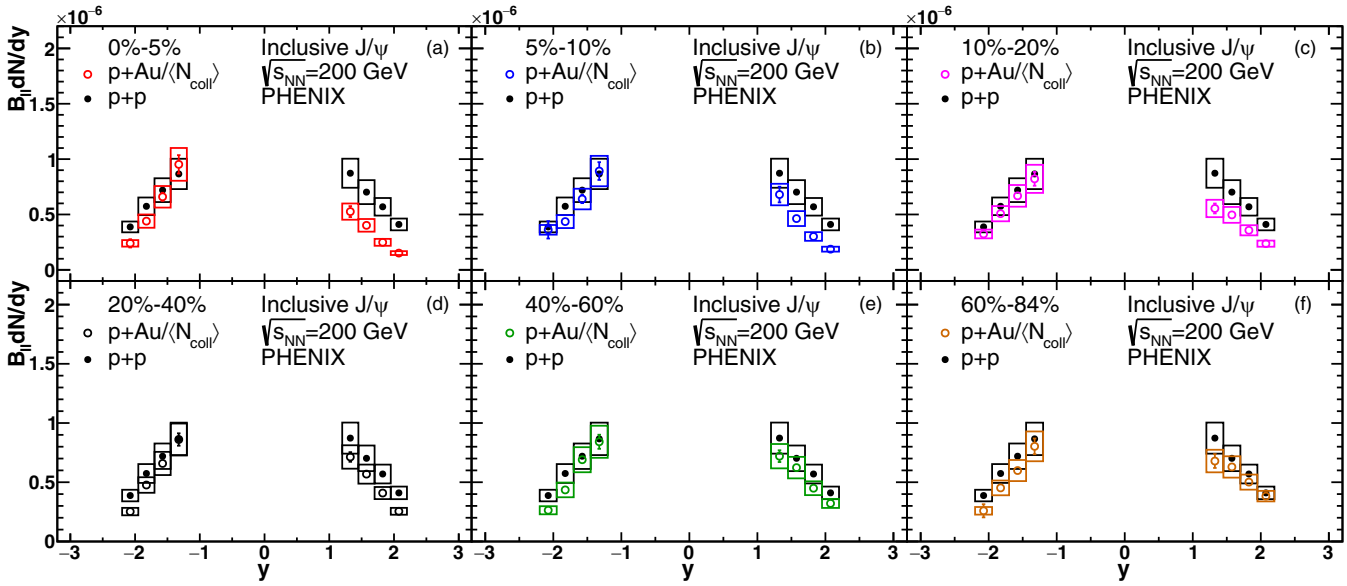

FIG. 24. J/ψ invariant yield as a function of y in various centrality bins of $p+$Au collisions. Bars (boxes) around data points represents point-to-point uncorrelated (correlated) uncertainties. There is also a global uncertainty of 11.9%, 11.8%, 12.2%, 12.1%, 12.2%, and 14.0% corresponding to 0%–5%, 5%–10%, 10%–20%, 20%–40%, 40%–60%, and 60%–84% centrality.

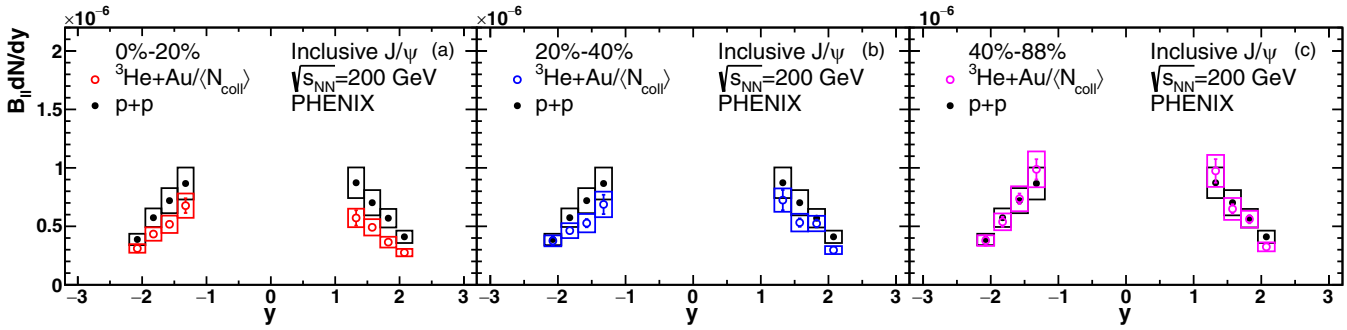

FIG. 25. J/ψ invariant yield as a function of y in various centrality bins of ^{3}He $+$Au collisions. Bars (boxes) around data points represents point-to-point uncorrelated (correlated) uncertainties. There is also a global uncertainty of 12.7%, 12.6%, and 13.4% corresponding to 0%–20%, 20%–40%, and 40%–88% centrality.

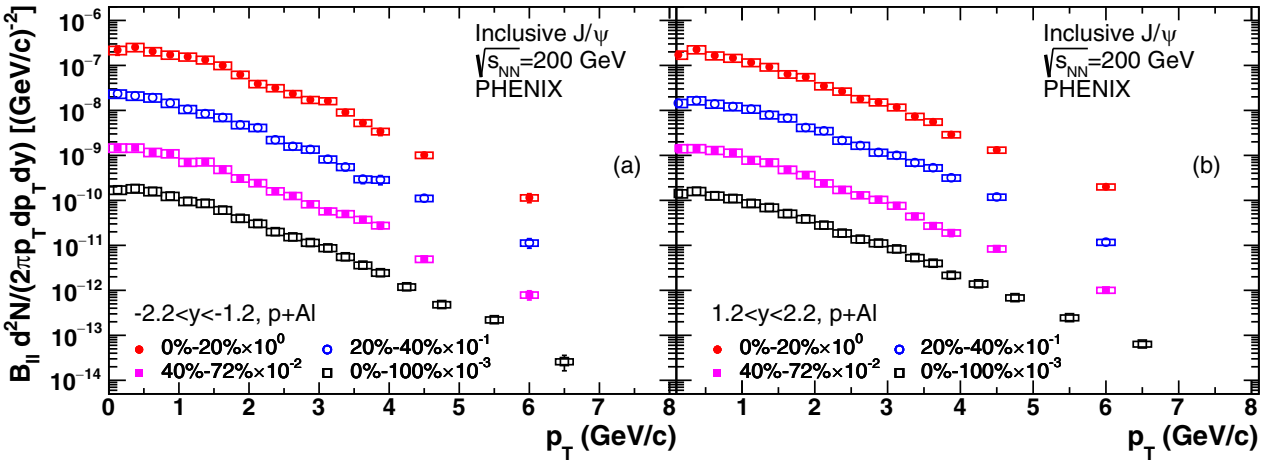

FIG. 26. J/ψ invariant yield as a function of p_T in various centrality bins of $p+$Al collisions, and the yields in each centrality bin are scaled for better visibility. Bars (boxes) around data points represents point-to-point uncorrelated (correlated) uncertainties. There is also a global uncertainty of 10.2%, 10.3%, 10.9%, and 10.4% corresponding to 0%–20%, 20%–40%, 40%–72%, and 0%–100% centrality.

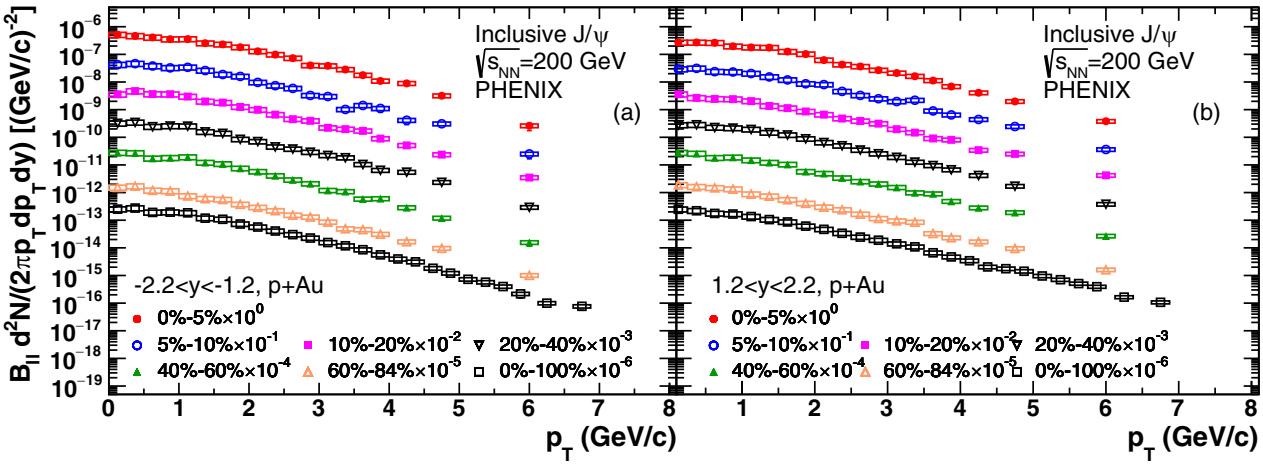

FIG. 27. J/ψ invariant yield as a function of p_T in various centrality bins of $p+$Au collisions, and the yields in each centrality bin are scaled for better visibility. Bars (boxes) around data points represents point-to-point uncorrelated (correlated) uncertainties. There is also a global uncertainty of 11.8% for 60%–84% centrality and 10.2% for all remaining centralities.

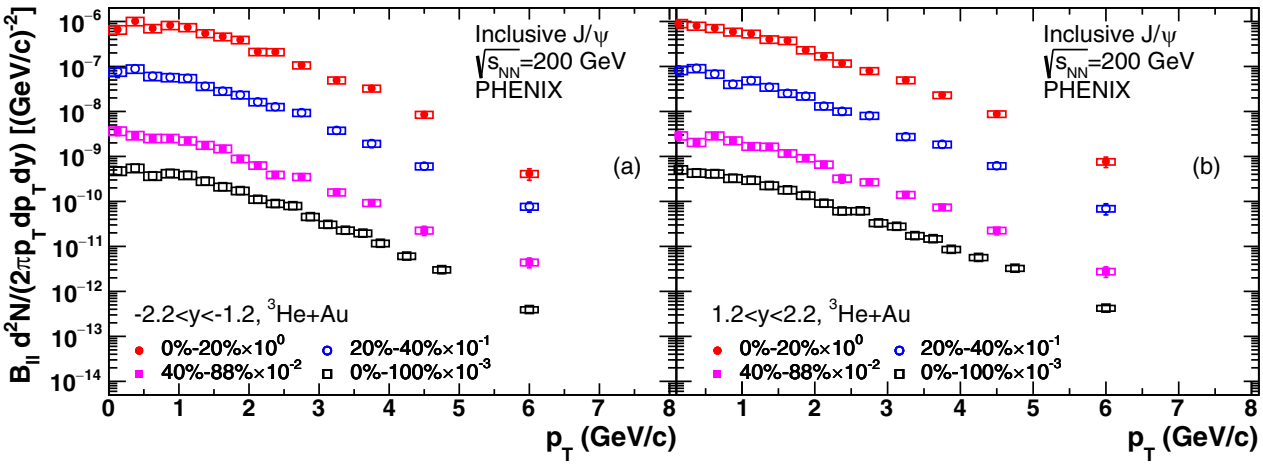

FIG. 28. J/ψ invariant yield as a function of p_T in various centrality bins of ^{3}He $+$Au collisions, and the yields in each centrality bin are scaled for better visibility. Bars (boxes) around data points represents point-to-point uncorrelated (correlated) uncertainties. There is also a global uncertainty of 10.7% for 40%–88% centrality and 10.2% for all remaining centralities.

TABLE IV. p_T bins in different data sets and centrality bins. All values are in GeV/c.

p+p	p+Al 0%–100%	p+Al Centrality	p+Au 0%–100%	p+Au Centrality	^{3}He +Au 0%–100%	^{3}He +Au Centrality
0.00–0.25	0.00–0.25	0.00–0.25	0.00–0.25	0.00–0.25	0.00–0.25	0.00–0.25
0.25–0.50	0.25–0.50	0.25–0.50	0.25–0.50	0.25–0.50	0.25–0.50	0.25–0.50
0.50–0.75	0.50–0.75	0.50–0.75	0.50–0.75	0.50–0.75	0.50–0.75	0.50–0.75
0.75–1.00	0.75–1.00	0.75–1.00	0.75–1.00	0.75–1.00	0.75–1.00	0.75–1.00
1.00–1.25	1.00–1.25	1.00–1.25	1.00–1.25	1.00–1.25	1.00–1.25	1.00–1.25
1.25–1.50	1.25–1.50	1.25–1.50	1.25–1.50	1.25–1.50	1.25–1.50	1.25–1.50
1.50–1.75	1.50–1.75	1.50–1.75	1.50–1.75	1.50–1.75	1.50–1.75	1.50–1.75
1.75–2.00	1.75–2.00	1.75–2.00	1.75–2.00	1.75–2.00	1.75–2.00	1.75–2.00
2.00–2.25	2.00–2.25	2.00–2.25	2.00–2.25	2.00–2.25	2.00–2.25	2.00–2.25
2.25–2.50	2.25–2.50	2.25–2.50	2.25–2.50	2.25–2.50	2.25–2.50	2.25–2.50
2.50–2.75	2.50–2.75	2.50–2.75	2.50–2.75	2.50–2.75	2.50–2.75	2.50–3.00
2.75–3.00	2.75–3.00	2.75–3.00	2.75–3.00	2.75–3.00	2.75–3.00	3.00–3.50
3.00–3.25	3.00–3.25	3.00–3.25	3.00–3.25	3.00–3.25	3.00–3.25	3.50–4.00
3.25–3.50	3.25–3.50	3.25–3.50	3.25–3.50	3.25–3.50	3.25–3.50	4.00–5.00
3.50–3.75	3.50–3.75	3.50–3.75	3.50–3.75	3.50–3.75	3.50–3.75	5.00–7.00
3.75–4.00	3.75–4.00	3.75–4.00	3.75–4.00	3.75–4.00	3.75–4.00	
4.00–4.25	4.00–4.50	4.00–5.00	4.00–4.25	4.00–4.50	4.00–4.50	
4.25–4.50	4.50–5.00	5.00–7.00	4.25–4.50	4.50–5.00	4.50–5.00	
4.50–4.75	5.00–6.00		4.50–4.75	5.00–7.00	5.00–7.00	
4.75–5.00	6.00–7.00		4.75–5.00			
5.00–5.25			5.00–5.25			
5.25–5.50			5.25–5.50			
5.50–5.75			5.50–5.75			
5.75–6.00			5.75–6.00			
6.00–6.50			6.00–6.50			
6.50–7.00			6.50–7.00			

[1] K. J. Eskola, P. Paakkinen, H. Paukkunen, and C. A. Salgado, EPPS16: Nuclear parton distributions with LHC data, Eur. Phys. J. C **77**, 163 (2017).

[2] K. Kovarik *et al.*, nCTEQ15- Global analysis of nuclear parton distributions with uncertainties in the CTEQ framework, Phys. Rev. D **93**, 085037 (2016).

[3] I. Vitev, Non-Abelian energy loss in cold nuclear matter, Phys. Rev. C **75**, 064906 (2007).

[4] D. C. McGlinchey, A. D. Frawley, and R. Vogt, Impact parameter dependence of the nuclear modification of J/ψ production in $d+$Au collisions at $\sqrt{s_{NN}} = 200$ GeV, Phys. Rev. C **87**, 054910 (2013).

[5] F. Arleo, P. B. Gossiaux, T. Gousset, and J. Aichelin, Charmonium suppression in pA collisions, Phys. Rev. C **61**, 054906 (2000).

[6] D. Kharzeev and K. Tuchin, Signatures of the color glass condensate in J/ψ production off nuclear targets, Nucl. Phys. A **770**, 40 (2006).

[7] H. Fujii, F. Gelis, and R. Venugopalan, Quark pair production in high energy pA collisions: General features, Nucl. Phys. A **780**, 146 (2006).

[8] J. W. Cronin, H. J. Frisch, M. J. Shochet, J. P. Boymond, P. A. Piroué, and R. L. Sumner, Production of hadrons at large transverse momentum at 200, 300, and 400 GeV, Phys. Rev. D **11**, 3105 (1975).

[9] A. Adare *et al.* (PHENIX Collaboration), Cold Nuclear Matter Effects on J/ψ Yields as a Function of Rapidity and Nuclear Geometry in Deuteron-Gold Collisions at $\sqrt{s_{NN}} = 200$ GeV, Phys. Rev. Lett. **107**, 142301 (2011).

[10] A. Adare *et al.* (PHENIX Collaboration), Transverse-momentum dependence of the J/ψ nuclear modification in $d+$Au collisions at $\sqrt{s_{NN}} = 200$ GeV, Phys. Rev. C **87**, 034904 (2013).

[11] A. Adare *et al.* (PHENIX Collaboration), Nuclear Modification of ψ', χ_c, and J/ψ Production in $d+$Au Collisions at $\sqrt{s_{NN}} =$ 200 GeV, Phys. Rev. Lett. **111**, 202301 (2013).

[12] A. Adare *et al.* (PHENIX Collaboration), Measurement of the relative yields of $\psi(2S)$ to $\psi(1S)$ mesons produced at forward and backward rapidity in $p+p$, $p+$Al, $p+$Au, and ^{3}He +Au collisions at $\sqrt{s_{NN}} = 200$ GeV, Phys. Rev. C **95**, 034904 (2017).

[13] L. Adamczyk *et al.* (STAR Collaboration), J/ψ production at low transverse momentum in $p+p$ and d+Au collisions at $\sqrt{s_{NN}} = 200$ GeV, Phys. Rev. C **93**, 064904 (2016).

[14] J. Adam *et al.* (ALICE Collaboration), Centrality dependence of inclusive J/ψ production in p-Pb collisions at $\sqrt{s_{\rm NN}} = 5.02$ TeV, J. High Energy Phys. 11 (2015) 127.

[15] B. B. Abelev *et al.* (ALICE Collaboration), J/ψ production and nuclear effects in p-Pb collisions at $\sqrt{s_{NN}} = 5.02$ TeV, J. High Energy Phys. 02 (2014) 073.

[16] B. B. Abelev *et al.* (ALICE Collaboration), Suppression of $\psi(2S)$ production in p-Pb collisions at $\sqrt{s_{NN}} = 5.02$ TeV, J. High Energy Phys. 12 (2014) 073.

[17] J. Adam *et al.* (ALICE Collaboration), Centrality dependence of $\psi(2S)$ suppression in p-Pb collisions at $\sqrt{s_{\rm NN}} = 5.02$ TeV, J. High Energy Phys. 06 (2016) 050.

[18] R Aaij *et al.* (LHCb Collaboration), Study of J/ψ production and cold nuclear matter effects in pPb collisions at $\sqrt{s_{NN}} =$ 5 TeV, J. High Energy Phys. 02 (2014) 072.

[19] R. Aaij *et al.* (LHCb Collaboration), Study of $\psi(2S)$ production and cold nuclear matter effects in pPb collisions at $\sqrt{s_{NN}} =$ 5 TeV, J. High Energy Phys. 03 (2016) 133.

[20] A. M Sirunyan *et al.* (CMS Collaboration), Measurement of prompt and nonprompt J/ψ production in pp and pPb collisions at $\sqrt{s_{\rm NN}} = 5.02$ TeV, Eur. Phys. J. C **77**, 269 (2017).

[21] A. M Sirunyan *et al.* (CMS Collaboration), Measurement of prompt $\psi(2S)$ production cross sections in proton-lead and proton-proton collisions at $\sqrt{s_{\rm NN}} = 5.02$ TeV, Phys. Lett. B **790**, 509 (2019).

[22] G. Aad *et al.* (ATLAS Collaboration), Measurement of differential J/ψ production cross sections and forward-backward ratios in $p+$ Pb collisions with the ATLAS detector, Phys. Rev. C **92**, 034904 (2015).

[23] M. Aaboud *et al.* (ATLAS Collaboration), Measurement of quarkonium production in proton-lead and proton-proton collisions at 5.02 TeV with the ATLAS detector, Eur. Phys. J. C **78**, 171 (2018).

[24] E. G. Ferreiro, Excited charmonium suppression in proton-nucleus collisions as a consequence of comovers, Phys. Lett. B **749**, 98 (2015).

[25] K. Dusling, W. Li, and B. Schenke, Novel collective phenomena in high-energy proton-proton and proton-nucleus collisions, Int. J. Mod. Phys. E **25**, 1630002 (2016).

[26] A. Adare *et al.* (PHENIX Collaboration), Quadrupole Anisotropy in Dihadron Azimuthal Correlations in Central $d+$Au Collisions at $\sqrt{s_{NN}} = 200$ GeV, Phys. Rev. Lett. **111**, 212301 (2013).

[27] A. Adare *et al.* (PHENIX Collaboration), Measurement of Long-Range Angular Correlation and Quadrupole Anisotropy of Pions and (Anti)Protons in Central $d+$Au Collisions at $\sqrt{s_{NN}} = 200$ GeV, Phys. Rev. Lett. **114**, 192301 (2015).

[28] X. Du and R. Rapp, Sequential regeneration of charmonia in heavy-ion collisions, Nucl. Phys. A **943**, 147 (2015).

[29] A. Beraudo, A. De Pace, M. Monteno, M. Nardi, and F. Prino, Heavy-flavour production in high-energy d-Au and p-Pb collisions, J. High Energy Phys. 03 (2016) 123.

[30] C. Aidala *et al.* (PHENIX Collaboration), Creation of quark-gluon plasma droplets with three distinct geometries, Nat. Phys. **15**, 214 (2019).

[31] J. D. Orjuela Koop, A. Adare, D. McGlinchey, and J. L. Nagle, Azimuthal anisotropy relative to the participant plane from a multiphase transport model in central $p+$Au, $d+$Au, and ^{3}He$+$Au collisions at $\sqrt{s_{NN}} = 200$ GeV, Phys. Rev. C **92**, 054903 (2015).

[32] A. Adare *et al.* (PHENIX Collaboration), Measurements of Elliptic and Triangular Flow in High-Multiplicity ^{3}He$+$Au Collisions at $\sqrt{s_{NN}} = 200$ GeV, Phys. Rev. Lett. **115**, 142301 (2015).

[33] K. Adcox *et al.* (PHENIX Collaboration), PHENIX detector overview, Nucl. Instrum. Methods Phys. Res. A **499**, 469 (2003).

[34] C. Aidala *et al.*, The PHENIX forward silicon vertex detector, Nucl. Instrum. Methods Phys. Res. A **755**, 44 (2014).

[35] H. Akikawa *et al.* (PHENIX Collaboration), PHENIX muon arms, Nucl. Instrum. Methods Phys. Res. A **499**, 537 (2003).

[36] S. Adachi *et al.*, Trigger electronics upgrade of PHENIX muon tracker, Nucl. Instrum. Methods Phys. Res. A **703**, 114 (2013).

[37] A. Drees, B. Fox, Z. Xu, and H. Huang, Results from Vernier scans at RHIC during the pp Run 2001–2002, Conf. Proc. C **030512**, 1688 (2003).

[38] S. S. Adler *et al.* (PHENIX Collaboration), Mid-Rapidity Neutral Pion Production in Proton Proton Collisions at $\sqrt{s} =$ 200 GeV, Phys. Rev. Lett. **91**, 241803 (2003).

[39] A. Adare *et al.* (PHENIX Collaboration), Centrality categorization for $R_{p(d)+A}$ in high-energy collisions, Phys. Rev. C **90**, 034902 (2014).

[40] C. Aidala *et al.* (PHENIX Collaboration), Measurements of $\mu\mu$ pairs from open heavy flavor and Drell-Yan in $p+p$ collisions at $\sqrt{s} = 200$ GeV, Phys. Rev. D **99**, 072003 (2019).

[41] A. Adare *et al.* (PHENIX Collaboration), Ground and excited charmonium state production in $p+p$ collisions at $\sqrt{s} = 200$ GeV, Phys. Rev. D **85**, 092004 (2012).

[42] J. E. Gaiser, Charmonium spectroscopy from radiative decays of the J/ψ and ψ', Ph.D. thesis, SLAC (1982).

[43] M. Tanabashi *et al.* (Particle Data Group), Review of particle physics, Phys. Rev. D **98**, 030001 (2018).

[44] A. Adare *et al.* (PHENIX Collaboration), Heavy quark production in $p+p$ and energy loss and flow of heavy quarks in Au+Au collisions at $\sqrt{s_{NN}} = 200$ GeV, Phys. Rev. C **84**, 044905 (2011).

[45] A. Adare *et al.* (PHENIX Collaboration), Detailed measurement of the e^+e^- pair continuum in $p+p$ and Au+Au collisions at $\sqrt{s_{NN}} = 200$ GeV and implications for direct photon production, Phys. Rev. C **81**, 034911 (2010).

[46] Y. H. Leung (PHENIX Collaboration), Measurements of charm, bottom, and Drell-Yan via dimuons in $p+p$ and $p+$Au collisions at $\sqrt{s_{NN}} = 200$ GeV with PHENIX at RHIC, Nucl. Phys. A **982**, 695 (2019).

[47] C. Aidala *et al.* (PHENIX Collaboration), Nuclear-modification factor of charged hadrons at forward and backward rapidity in $p+$Al and $p+$Au collisions at $\sqrt{s_{NN}} = 200$ GeV, Phys. Rev. C **101**, 034910 (2020).

[48] S. Agostinelli *et al.* (GEANT4 Collaboration), GEANT4: A simulation toolkit, Nucl. Instrum. Methods Phys. Res. A **506**, 250 (2003).

[49] T. Sjöstrand, S. Mrenna, and P. Z. Skands, A brief introduction to PYTHIA 8.1, Comput. Phys. Commun. **178**, 852 (2008).

[50] R. Vogt, Shadowing effects on J/ψ and Υ production at energies available at the CERN Large Hadron Collider, Phys. Rev. C **92**, 034909 (2015).

[51] R. E. Nelson, R. Vogt, and A. D. Frawley, Narrowing the uncertainty on the total charm cross section and its effect on the J/ψ cross section, Phys. Rev. C **87**, 014908 (2013).

[52] A. Kusina, J.-P. Lansberg, I. Schienbein, and H.-S. Shao, Gluon Shadowing in Heavy-Flavor Production at the LHC, Phys. Rev. Lett. **121**, 052004 (2018).

[53] H.-S. Shao, HELAC-Onia: An automatic matrix element generator for heavy quarkonium physics, Comput. Phys. Commun. **184**, 2562 (2013).

[54] H.-S. Shao, HELAC-Onia 2.0: An upgraded matrix-element and event generator for heavy quarkonium physics, Comput. Phys. Commun. **198**, 238 (2016).

[55] J.-P. Lansberg and H.-S. Shao, Towards an automated tool to evaluate the impact of the nuclear modification of the gluon density on quarkonium, D and B meson production in proton-nucleus collisions, Eur. Phys. J. C **77**, 1 (2017).

[56] X. Zhao and R. Rapp, Charmonium in medium: From correlators to experiment, Phys. Rev. C **82**, 064905 (2010).

[57] X. Du and R. Rapp, In-medium charmonium production in proton-nucleus collisions, J. High Energy Phys. 03 (2019) 015.

[58] C. Loizides, J. Nagle, and P. Steinberg, Improved version of the PHOBOS Glauber Monte Carlo, SoftwareX **1-2**, 13 (2015).

[59] K. J. Eskola, H. Paukkunen, and C. A. Salgado, EPS09: A new generation of NLO and LO nuclear parton distribution functions, J. High Energy Phys. 04 (2009) 065.

[60] X. Zhao and R. Rapp, Forward and midrapidity charmonium production at RHIC, Eur. Phys. J. C **62**, 109 (2009).

[61] A. Adare *et al.* (PHENIX Collaboration), Pseudorapidity Dependence of Particle Production and Elliptic Flow in Asymmetric Nuclear Collisions of $p+\mathrm{Al}$, $p+\mathrm{Au}$, $d+\mathrm{Au}$, and $^3\mathrm{He}+\mathrm{Au}$ at $\sqrt{s_{NN}} = 200$ GeV, Phys. Rev. Lett. **121**, 222301 (2018).